Journal of Wind Engineering & Industrial Aerodynamics xxx (xxxx) xxx

Contents lists available at ScienceDirect

Journal of Wind Engineering & Industrial Aerodynamics

journal homepage: www.elsevier.com/locate/jweia

Potential and challenges of wind measurements using met-masts in complex topography for bridge design: Part II – Spectral flow characteristics

Zakari Midjiyawa [a,b,*], Etienne Cheynet [c], Joachim Reuder [c], Hálfdán Ágústsson [d], Trond Kvamsdal [b]

[a] Norwegian Meteorological Institute, Henrik Mohns Plass 1, 0313, Oslo, Norway
[b] Department of Mathematical Sciences, Norwegian University of Science and Technology, Alfred Getz' vei 1, 7491, Trondheim, Norway
[c] Geophysical Institute and Bergen Offshore Wind Centre, University of Bergen, Allegaten 70, 5007, Bergen, Norway
[d] Kjeller Vindteknikk, Norconsult AS, Tærudgata 16, Lillestrøm, Norway

ARTICLE INFO

Keywords:
Bridges
Meteorological mast
Turbulence spectrum
Coherence
Complex terrain
Sonic anemometer

ABSTRACT

This study quantifies the influence of the local topography on sonic anemometer measurements mounted on tall met-masts deployed in Norwegian fjords. This assessment is done by analysing the second-order structure of turbulence in the frequency space. The objective is to evaluate how the data collected by these masts can help with the design of future fjord-crossing bridges. Using measurements from eight masts deployed in three different fjords, spectral characteristics common to the different locations were identified. Among the characteristics investigated, the one-point velocity spectra and the vertical coherence of turbulence are of special interest for bridge design. Using only situations with a mean wind speed of 12 m s^{-1} and above and rather stationary flow conditions, the remaining wind direction sectors could be classified into two main groups: those with a long fetch over smooth topography and those with a rough heterogeneous terrain upstream of the masts. It was found that if the velocity spectra are normalized by an appropriate estimate of the friction velocity, surface-layer scaling may be applicable in Norwegian fjords, at least under near-neutral conditions. The velocity spectra, estimated with long upstream fjord fetches have characteristics consistent with those collected in coastal and offshore environments. The Davenport model showed limited capabilities in describing the co-coherence of turbulence on vertical separations. The dependency of the Davenport decay coefficient with the height and spatial separation is highlighted and may be substantial in mountainous terrain. Although the spectral flow characteristics estimated on the shore of fjords are relevant for the design of fjord-crossing bridge towers, they may not easily be extrapolated for the modelling of the turbulent flow in the middle of the fjord. Nevertheless, they are still valuable to complement computational fluid dynamic simulations, wind tunnel tests, or remote sensing of wind across the fjord.

1. Introduction

The characterization of the wind conditions in fjords by tall met-masts can be particularly challenging. Midjiyawa et al. (2021) showed, for example, that high wind speeds are often recorded for only a limited number of narrow sectors and that the flow characteristics at the mast locations might differ significantly from those in the middle of the fjord.

However, the local topography may not equally affect eddies of different sizes. Deviations of the estimated integral flow characteristics from those in flat terrain were observed in Midjiyawa et al. (2021). These may be linked to a perturbation of the low-frequency turbulence fluctuations by the local terrain while the high-frequency range may remain less affected (Frank, 1996). An investigation of the spectral structure of turbulence is, therefore, vital to identify to what extent the records from the masts on the shore can be used to model the velocity spectra and coherence of turbulence above the water in narrow fjords. The present paper complements the study by Midjiyawa et al. (2021) by focusing on the second-order spectral characteristics of turbulence, which is relevant for the design of long-span bridges.

The one-point spectra and coherence are fundamental to calculate turbulent wind loading on long-span bridges (Scanlan, 1978; Davenport, 1961b). Full-scale studies, focusing on the spectral characteristics of turbulence for bridge design, are typically site-specific (Hui et al., 2009; Cheynet et al., 2016; Fenerci et al., 2017; Yu et al., 2019; Song et al.,

* Corresponding author. Norwegian Meteorological Institute, Henrik Mohns Plass 1, 0313, Oslo, Norway.
E-mail address: midjiyawaz@met.no (Z. Midjiyawa).

https://doi.org/10.1016/j.jweia.2021.104585
Received 26 October 2020; Received in revised form 20 January 2021; Accepted 17 February 2021
Available online xxxx

2020). Whereas turbulence characteristics in complex terrain are undoubtedly affected by the local topography, there may exist common features between multiple sites in a specific type of topography, for example, a fjord. Identifying such shared features is thus of major interest when modelling the dynamic wind load on fjord-crossing bridges. In this regard, a systematic characterization of turbulence from multiple sites is desirable, but unfortunately rarely done.

As the need for long-span bridges in mountainous environments increases (Table 1), turbulence spectra and coherence models appropriate to model the dynamic wind load in rough terrains are required. One-point spectral models (e.g. Busch and Panofsky, 1968; Kaimal et al., 1972; Tieleman, 1995; von Kármán, 1948; Simiu and Scanlan, 1996) and coherence models (Davenport, 1961b) commonly found in the literature were originally established in flat and homogeneous topographies. Their applicability in mountainous terrain, as in fjords, is still unclear.

This paper aims to identify potential common features of turbulence in the frequency space by focusing on two sectors in each fjord, characterized by converse flow conditions: long-fetch winds, defined as winds blowing over an extended stretch of water, typically more than 2 km; and short-fetch winds, defined as winds blowing over irregular and heterogeneous terrain upstream of the measurement location. Furthermore, the study aims at exploring the variation of the co-coherence of turbulence between the different fjords. It also reassesses the applicability of the widely used Davenport model in complex topography.

The rest of the paper is organized as follows; Section 2 discusses the choice of scaling velocity and length in the surface layer. The section further introduces the different co-coherence models. Section 4 presents the methods and assumptions used in the estimation of velocity spectra and co-coherence. Section 5 discusses the influence of topography on the velocity spectra and spectral ratios as well as on the spatial correlation of turbulence.

2. Fundamentals of turbulence and turbulence-induced wind load

2.1. Choice of the scaling velocity and scaling length

As in Midjiyawa et al. (2021), atmospheric turbulence is modelled as a three-variate, three-dimensional correlated random process $\{u, v, w\}$ in a coordinate system $\{x, y, z\}$, where x, y and z denote the along-wind, cross-wind and vertical directions, respectively.

In both wind engineering and micro-meteorology, the velocity spectra are scaled by a characteristic length and velocity. Following Monin-Obukhov Similarity Theory (MOST) (Monin and Obukhov, 1954), the scaling velocity is the friction velocity u_*, whereas the scaling length is the height z above the ground. MOST is applicable only in the surface layer, i.e. roughly the lower 10% of the atmospheric boundary layer. Although u_* and z are sporadically used in wind engineering (e.g. Simiu and Scanlan, 1996), other characteristic lengths and velocity scaling are more common. In Dyrbye and Hansen (1997) or EN 1991-1-4 (2005), the spectrum of the along-wind velocity component is of special interest. For this component, the scaling velocity is the standard deviation of the along-wind component σ_u, whereas the scaling length is the integral length scale L_u^x, which is modelled as a non-linear function of z.

Following Dyrbye and Hansen (1997), the use of L_u^x aims to account for the inadequacy of MOST at altitudes above 50 m, which is a reasonable motivation. However, the literature supporting the use of the integral length scale as scaling length is rather scarce, while full-scale measurements indicated that, under neutral conditions, z is still appropriate at heights above 80 m above the surface (e.g. Mikkelsen et al. (2017); Cheynet et al., 2018). Although the integral length scale is a key characteristic in wind-tunnel tests, its estimation in an outdoor environmentis prone to significant error and its usefulness to study atmospheric turbulence is thus questionable (Panosfsky and Dutton, 1984). The integral length scales are used in the von Kármán spectrum (von Kármán, 1948; Morfiadakis et al., 1996) and the ESDU spectrum model (ESDU, 2001). However, the length scale is reliable only if the spectral peak is clearly defined (Cheynet et al., 2018), which is rarely the case in the atmospheric boundary layer, especially close to the ground, where the spectral peak can be flat (Högström et al., 2002). Natural wind includes also a combination of submeso-, meso- and microscale fluctuations, which are not accounted for in wind tunnel tests or spectral tensor models (e.g Mann, 1994), which further challenges the estimation of the integral length scales. For these reasons, the von Kármán spectrum is not discussed herein. Besides, in the upper part of the atmospheric boundary layer, the thickness of the boundary layer acts as the scaling length (Högström et al., 2002), such that the turbulence spectrum is independent of the altitude, meaning that both z and L_u^x become inappropriate above a given height. In the present case, the simultaneous presence of mountains and the sea challenge the choice of an adequate boundary layer height. As the measurements were conducted in the first 100 m above the ground, it was decided to use z as a scaling length.

In the inertial subrange, Kaimal et al. (1972) derived some asymptotic relations for the normalized power spectral densities (PSDs) of the three velocity components.

$$\frac{fS_u(f)}{u_*^2} \sim 0.3 f_r^{-\frac{2}{3}} \quad \text{at} \quad f_r \gg 1 \tag{1}$$

$$\frac{fS_v(f)}{u_*^2} \simeq \frac{fS_w(f)}{u_*^2} \sim 0.4 f_r^{-\frac{2}{3}} \quad \text{at} \quad f_r \gg 1 \tag{2}$$

$$f_r = \frac{fz}{\overline{u}} \tag{3}$$

where S_u, S_v and S_w are the along-wind, cross-wind and vertical velocity spectra, respectively; f is the frequency and u is the horizontal mean wind speed. Equations (1) and (2) satisfy the hypothesis of local isotropy in the inertial subrange (Kolmogorov, 1941)

$$\frac{S_w}{S_u} \simeq \frac{S_v}{S_u} \sim \frac{4}{3} \quad \text{at} \quad f_r \gg 1 \tag{4}$$

Equations (1) and (2) are of major importance to assess the quality of the anemometer records, for example, to know if flow distortion occurs (Cheynet et al., 2019; Peña et al., 2019). The ratios S_w/S_u and S_v/S_u can also be affected by aliasing if the velocity data are recorded with a relatively low sampling frequency or if the data have been decimated without the application of a low-pass filter. Failure to satisfy eq. (4) may also indicate that the inertial subrange has not yet been reached by the S_w

Table 1
Long-span cable-suspended bridges built in mountainous terrain (main span larger than 600 m).

Year	Name	Main span (m)	Location
2020	Jinshajiang Hutiaoxia Bridge	766	China
2020	Honghe Jianyuan Bridge	700	China
2020	Jin'an Bridge	1386	China
2018	Xingkang Bridge	1100	China
2018	Chajiaotan Bridge	1200	China
2018	Hålogaland Bridge	1145	Norway
2018	Sunxihe Bridge	660	China
2016	Longjiang River Bridge	1196	China
2016	Yachi Bridge	800	China
2016	Duge Bridge	720	China
2015	Qingshui River Bridge	1130	China
2015	Puli Bridge	628	China
2013	Hardanger Bridge	1310	Norway
2013	Lishui River Bridge	856	China
2012	Aizhai Bridge	1176	China
2009	Sidu River Bridge	900	China
2009	Baling River Bridge	1088	China
2009	Beipanjiang River Bridge	636	China
1992	Gjemnessund Bridge	623	Norway

or S_v spectrum because of the limited sampling frequency or the sonic-path averaging of the anemometer (Chamecki and Dias, 2004).

Using u_* as the velocity scale together with a logarithmic mean wind speed profile implies that the turbulence intensity is not explicitly used to compute the wind load. For a given velocity spectrum, the turbulence intensity can be modified by changing the roughness length z_0 or the reference mean wind speed u_{ref} at a reference height z_{ref}. Therefore, the along-wind dynamic wind load in one point can be modelled using only five parameters: $\{u_*, z_0, u_{ref}, z_{ref}, fS_u/u_*^2\}$, where fS_u/u_*^2 can be derived from Kaimal et al. (1972), Simiu and Scanlan (1996) or Tieleman (1995).

The friction velocity requires knowledge of the three velocity components and is associated with a larger statistical uncertainty than their standard deviation. The standard deviation of the along-wind velocity σ_u, may, therefore, appear as an attractive alternative velocity scale. Nevertheless, the use of σ_u requires an additional relation between u_* and σ_u, which is often approximated as $\sigma_u = Ku_*$ where K is a coefficient that depends on the terrain roughness (Simiu and Scanlan, 1996; Solari and Piccardo, 2001). This makes the relation between σ_u and u_* prone to large uncertainties in mountainous regions (e.g. de Franceschi et al., 2009; Midjiyawa et al., 2021). If surface-layer scaling is adopted, turbulence modelling with σ_u as scaling velocity leads to more parameters than necessary to compute the wind load. Besides, if the relation between σ_u and u_* is not carefully chosen, it is possible to simulate a flow field that does not satisfy eqs. (1) and (2), which is not desirable for a realistic simulation of an undisturbed turbulence field. In the present case, u_* was chosen as the scaling velocity based on data collected from 3D sonic anemometers and an averaging interval of 30 min was selected to reduce the statistical uncertainties.

The friction velocity is estimated hereafter using three different methods. First is the traditional approach, suggested by e.g. Weber (1999).

$$u_{*C} = \left[\overline{u'w'}^2 + \overline{v'w'}^2\right]^{1/4} \tag{5}$$

Second is the method by Klipp (2018).

$$u_{*R} = \left[(\lambda_1 - \lambda_3)\cos(\beta)\sin(\beta)\right]^{1/2} \tag{6}$$

where λ_1 and λ_3 are the largest and smallest principal components of the Reynolds stress tensor, respectively; β is defined as

$$\beta = 90 - \arccos\left(\frac{\boldsymbol{U}\cdot\boldsymbol{\Lambda_3}}{|\boldsymbol{U}|\,|\boldsymbol{\Lambda_3}|}\right) \tag{7}$$

where $\boldsymbol{\Lambda_3}$ is the eigenvector associated to λ_3 and $\boldsymbol{U}$ is the mean wind velocity vector. The third method incorporates also the horizontal covariance term of the Reynolds stress tensor

$$u_{*M} = \left[\overline{u'w'}^2 + \overline{u'v'}^2 + \overline{v'w'}^2\right]^{1/4} \tag{8}$$

The third method may be justified if $\overline{u'v'}$ contributes considerably to the surface stresses. However, eq. (8) should be interpreted with caution as its expression is not consistent with the properties of the Reynolds stress tensor (Klipp and Adelphi, 2008). Therefore eq. (8) is considered only when the other two methods to compute the friction velocity result in non-dimensional spectra that do not satisfy eqs. (1) and (2). Investigating eq. (8) is valuable to assess the appropriateness of u_* as the scaling velocity in a fjord-like topography.

For comparison purposes, the estimated PSDs are compared to the one-point auto and cross-spectral densities by Kaimal and Finnigan (1994), defined as.

$$\frac{fS_u(f)}{u_*^2} = \frac{102f_r}{(1+33f_r)^{\frac{5}{3}}} \tag{9}$$

$$\frac{fS_v(f)}{u_*^2} = \frac{17f_r}{(1+9.5f_r)^{\frac{5}{3}}} \tag{10}$$

$$\frac{fS_w(f)}{u_*^2} = \frac{2f_r}{1+5(f_r)^{\frac{5}{3}}} \tag{11}$$

$$\frac{f\mathrm{Re}(S_{uw}(f))}{u_*^2} = -\frac{14f_r}{(1+9.6f_r)^{\frac{7}{3}}} \tag{12}$$

where $\mathrm{Re}(S_{uw}(f))$ refers to the real part of the cross-spectrum. Since the terrain is heterogeneous, the anemometers may be located in different internal boundary layers. Therefore, the friction velocity is unlikely to be constant with the measurement height. Using local similarity theory (Sorbjan, 1986), it is possible to normalize the velocity spectra and cross-spectra based on local estimates of u_* instead of using the value at the lowest height. Following Figueroa-Espinoza and Salles (2014), this approach may be suitable in a mountainous environment and is, therefore, adopted in the following.

2.2. Surface-layer velocity spectra in complex terrains

Fig. 1 illustrates the fact that, in the surface layer, the maximal value of the normalized along-wind velocity spectrum is $fS_u/u_*^2 \approx 1$ (Kaimal et al., 1972; Högström et al., 2002). In the lower part of the surface layer, the strong shear and the blocking by the surface distort the eddies as they impinge and scrap along the surface (Högström et al., 2002; Hunt and Morrison, 2000; Hunt and Carlotti, 2001; Mikkelsen et al., 2017). This phenomenon leads to the distortion of the low-frequency range of the velocity spectrum. In particular, the spectral peak of the velocity spectrum pre-multiplied with the frequency flattens (left panel of Fig. 1) to create a "plateau" (Drobinski et al., 2004). Although the plateau is often observed in the first 30 m above the ground (Högström et al., 2002), it likely exists at higher altitudes (Drobinski et al., 2004). A practical tool to quantify blocking is to compare the imaginary part and real part of the cross-spectrum S_{uw} (Mann, 1994; Cheynet, 2018). If $\mathrm{Im}(S_{uw})$ is substantially different from zero, the blocking by the surface may not be negligible.

If u_* is the appropriate scaling velocity, an underestimation of its value will lead to a PSD estimate that lies systematically above eqs. (1)

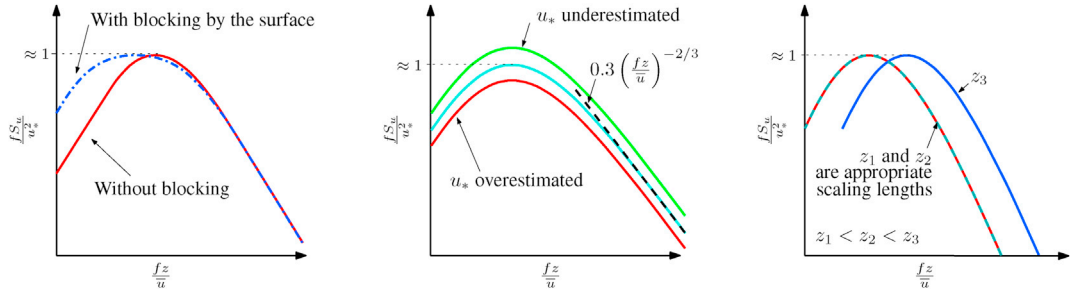

Fig. 1. Sketches of the normalized S_u velocity spectra highlighting the influence of the blockage by the surface on the width of the spectral peak (left panel), the value of the friction velocity estimate on the amplitude of the peak (middle panel) and the influence of the scaling length on the frequency at which the peak is reached.

and (2). Such an underestimation can be observed if u' v' substantially affects the turbulent shear stresses. If the altitude above the ground is no longer the adequate scaling length, the peaks of the normalized velocity spectra will be located at different frequencies when expressed as a function of f_r (right panel of Fig. 1). In summary, the scaling velocity governs the position of the normalized spectra on the ordinate, whereas the scaling length governs its position on the abscissa.

2.3. Modelling of the co-coherence

The normalized cross-spectrum of turbulence gives the spatial correlation of turbulence in the frequency space (Ropelewski et al., 1973). The root-coherence is defined as

$$\gamma_i(z_1, z_2, f) = \frac{S_i(z_1, z_2, f)}{\sqrt{S_i(z_1) S_i(z_2)}} \tag{13}$$

where $i = \{u, v, w\}$; $S_i(z_1)$ and $S_i(z_2)$ are the one-point spectra estimated at heights z_1 and z_2, respectively and $S_i(z_1, z_2, f)$ is the two-point cross-spectral density estimate between the anemometers at the heights z_1 and z_2. Equation (13) is a complex-valued function, the real part of which is called the co-coherence, whereas its imaginary part is called the quad-coherence.

In wind engineering, wind energy or boundary layer micro-meteorology, the co-coherence is often modelled using the so-called Davenport model (Davenport, 1961b).

$$\gamma_i(z_1, z_2, f) = \exp(-C^i f_D) \tag{14}$$

$$f_D = \frac{f|z_1 - z_2|}{\overline{u}(z_1, z_2)} \tag{15}$$

$$\overline{u}(z_1, z_2) = \frac{\overline{u}(z_1) + \overline{u}(z_2)}{2} \tag{16}$$

where $i = \{u, v, w\}$ and C^i is an empirical decay coefficient. Similarly to the one-point spectrum, the Davenport model was established in flat, and homogeneous terrain and relatively small separation distances. The Davenport model assumes that the decay coefficient (C^i) is constant. In contrast, Kanda and Royles (1978); Kanda (1983); Bowen et al. (1983) have proposed alternatives approaches of modelling vertical coherence which include the height above the surface. The model by Bowen et al. (1983) assumes that C^i depends on the height and the vertical separation between anemometers, such that.

$$C^i = C_1^i + C_2^i \frac{z_1 - z_2}{\overline{z}} \tag{17}$$

$$\overline{z} = \frac{z_1 + z_2}{2}. \tag{18}$$

To account for the fact that the coherence does not equal unity at zero frequency (Kristensen and Jensen, 1979), an additional decay parameter C_3^i is introduced in eq. (17) such that the co-coherence is finally modelled as.

$$\gamma_i(z_1, z_2, f) = A(z_1, z_2, f) \cdot \exp\left(-\frac{2C_3^i f |z_1 - z_2|^2}{(z_1 + z_2)\overline{u}(z_1, z_2)}\right) \tag{19}$$

$$A(z_1, z_2, f) = \exp\left(-\frac{|z_1 - z_2|}{\overline{u}(z_1, z_2)} \sqrt{(C_1^i f)^2 + (C_3^i)^2}\right) \tag{20}$$

The third parameter C_3^i has the dimension of the inverse of a time scale of turbulence. It is lower for the horizontal component compared to the vertical one because the turbulence length scales of the w component are generally smaller than for the u and v components (Solari and Piccardo, 2001). Furthermore, the introduction of C_3^i reduces the bias in the estimation of C_1^i and C_2^i. Additionally, if the low-frequency records are used without C_3^i, the co-coherence will be equal to 1 when $f = 0$ Hz, which is not realistic for large spatial separations. In this study, eq. (19) is used to illustrate the limits of the Davenport model to describe the vertical co-coherence of turbulence.

3. Observation setup and data processing

The fjords of interest are Sulafjorden, Halsafjorden and Julsundet located on the west coast of Norway. As a part of the E39-project, four masts were deployed in Sulafjorden, two in Halsafjorden and two others in Julsundet (Furevik et al., 2020; Midjiyawa et al., 2021). The two masts located on the northern part of Sulafjorden are installed on each side of the fjord and are labelled SulaNW and SulaNE. The masts on the southern area are named SulaSW and SulaSE. On the western and eastern sides of Halsafjorden and Julsundet, the masts deployed are named herein HalsaW/HalsaE and JulW/JulE, respectively. For the sake of brevity, the mast names, heights, types and coordinate location are summarised in Table 2. The reader is referred to Furevik et al. (2020) and Midjiyawa et al. (2021) for a detailed description of the measurement setup as well as the topography at the mast locations. Each mast was equipped with three to four 3D sonic anemometers (Gill WindMaster Pro). In total, two years (2018–2019) of data from 25 anemometers are used in the current study. The data were saved at a sampling frequency of 10 Hz and pre-processed as described in Midjiyawa et al. (2021). The key processing steps were.

- Samples with a mean wind speed lower than 12 m s^{-1} were discarded to ensure that the majority of the records are representative of near-neutral conditions.
- The double rotation technique was used for anemometer tilt correction.
- Linear trends were removed to study turbulent fluctuations.
- Highly non-Gaussian, non-stationary fluctuations and samples characterized with high statistical uncertainties in the momentum flux were removed.

4. Methodology for spectral analysis

The selected data were organized into stationary time series of 30 min. The one-point auto and cross-spectral densities of the velocity fluctuations were estimated using Welch's algorithm (Welch, 1967) with

Table 2
Overview of the met-masts: Mast acronym, mast location, mast height, mast type, sensor heights, boom orientation, boom length, and coordinate position. Reproduced from Midjiyawa et al. (2021).

Mast acro.	Mast loc.	Mast h.(m)	Mast type	Sensor h. (m)	Boom orient. (Deg)	Boom l. (m)	Coord.(UTM32)
SulaNW	Kvitneset	100.5	Lattice	92.5, 71.5, 44.5	72, 74, 74	6.1	6924741 N, 345142 E
SulaNE	Trælbodneset	78.0	Lattice	76.8, 48.3, 27.3	289, 290, 290	6.1	6925267 N, 348347 E
SulaSW	Langeneset	97.0	Lattice	94.8, 75.0, 50.0, 27.0	81, 81, 81, 81	4.4	6920740 N, 346520 E
SulaSE	Kårsteinen	63.0	Lattice	62.8, 40.0, 13.4	223, 223, 223	3.6	6922074 N, 351140 E
HalsaW	Halsaneset	50	Tubular	50.3, 31.9, 12.7	106, 106, 104	1.8	6995095 N, 456472 E
HalsaE	Åkvik	50	Lattice	48.3, 31.9, 17.0	227, 227, 227	4	6995697 N, 458519 E
JulW	Nautneset	68	Lattice	68.3, 52.3, 32.7	239, 239, 239	5.1	6957381 N, 394634 E
JulE	Julbo	50	Tubular	50.3, 31.9, 12.7	234, 234, 234	1.8	6957730 N, 396210 E

Table 3
Normalized standard deviation and turbulence intensity for long-fetch winds. The anemometer closest to 50 m above ground is chosen.

Mast	Sector (°)	σ_w/u_{*C}	σ_v/u_{*C}	σ_u/u_{*C}	σ_w/σ_u	σ_v/σ_u	I_u	I_v	I_w
SulaNW	300–330	1.41 ± 0.19	2.39 ± 0.56	2.09 ± 0.38	0.68 ± 0.10	1.15 ± 0.24	0.08 ± 0.02	0.09 ± 0.03	0.05 ± 0.01
	135–165	1.97 ± 0.34	2.37 ± 0.42	2.62 ± 0.51	0.76 ± 0.09	0.92 ± 0.14	0.13 ± 0.02	0.11 ± 0.02	0.10 ± 0.02
SulaNE	150–210	1.76 ± 0.30	2.81 ± 0.56	2.65 ± 0.51	0.67 ± 0.09	1.07 ± 0.17	0.10 ± 0.02	0.11 ± 0.03	0.07 ± 0.02
	300–20	1.71 ± 0.33	2.35 ± 0.71	2.40 ± 0.52	0.72 ± 0.10	0.97 ± 0.17	0.13 ± 0.03	0.13 ± 0.04	0.09 ± 0.03
HalsaW	150–180	1.42 ± 0.20	2.32 ± 0.42	2.64 ± 0.43	0.54 ± 0.06	0.88 ± 0.12	0.10 ± 0.02	0.09 ± 0.02	0.05 ± 0.01
HalsaE	150–180	1.57 ± 0.29	2.61 ± 0.52	2.91 ± 0.62	0.55 ± 0.05	0.91 ± 0.11	0.11 ± 0.03	0.10 ± 0.02	0.06 ± 0.01
	300–360	1.39 ± 0.27	2.45 ± 0.48	2.55 ± 0.58	0.56 ± 0.08	0.98 ± 0.16	0.17 ± 0.02	0.15 ± 0.03	0.10 ± 0.01
JulW	120–195	1.46 ± 0.29	2.76 ± 0.53	2.62 ± 0.65	0.57 ± 0.10	1.08 ± 0.20	0.09 ± 0.04	0.10 ± 0.04	0.05 ± 0.03
JulE	120–195	1.65 ± 0.27	2.65 ± 0.68	2.74 ± 0.55	0.61 ± 0.11	0.97 ± 0.17	0.11 ± 0.02	0.11 ± 0.03	0.07 ± 0.02
	300–360	1.21 ± 0.13	2.32 ± 0.59	2.25 ± 0.40	0.55 ± 0.08	1.04 ± 0.22	0.10 ± 0.02	0.10 ± 0.03	0.05 ± 0.01

Table 4
Normalized standard deviation and turbulence intensity for short-fetch winds. The anemometer closest to 50 m above ground is chosen.

Mast	Sector (°)	σ_w/u_{*C}	σ_v/u_{*C}	σ_u/u_{*C}	σ_w/σ_u	σ_v/σ_u	I_u	I_v	I_w
SulaNW	165–185	1.98 ± 0.33	1.83 ± 0.35	2.32 ± 0.42	0.85 ± 0.07	0.79 ± 0.07	0.17 ± 0.03	0.13 ± 0.02	0.14 ± 0.02
SulaSW	135–165	1.68 ± 0.24	1.44 ± 0.12	1.81 ± 0.17	0.93 ± 0.12	0.80 ± 0.09	0.22 ± 0.03	0.17 ± 0.03	0.20 ± 0.04
	285–315	1.77 ± 0.24	1.72 ± 0.33	2.19 ± 0.27	0.81 ± 0.07	0.79 ± 0.15	0.18 ± 0.03	0.14 ± 0.04	0.15 ± 0.02
SulaSE	270–330	1.47 ± 0.23	1.96 ± 0.42	2.16 ± 0.38	0.69 ± 0.09	0.92 ± 0.18	0.14 ± 0.04	0.12 ± 0.03	0.10 ± 0.03
HalsaW	285–360	1.52 ± 0.26	2.43 ± 0.70	2.74 ± 0.74	0.57 ± 0.08	0.89 ± 0.12	0.18 ± 0.05	0.16 ± 0.04	0.11 ± 0.04
HalsaE	210–285	1.52 ± 0.17	2.41 ± 0.31	2.61 ± 0.27	0.59 ± 0.05	0.93 ± 0.10	0.17 ± 0.02	0.15 ± 0.03	0.10 ± 0.01
JulW	330–360	1.58 ± 0.23	2.04 ± 0.48	2.51 ± 0.35	0.63 ± 0.08	0.81 ± 0.12	0.15 ± 0.04	0.12 ± 0.03	0.10 ± 0.04
JulE	210–285	1.80 ± 0.32	2.44 ± 0.47	2.84 ± 0.49	0.64 ± 0.05	0.86 ± 0.09	0.18 ± 0.03	0.16 ± 0.03	0.12 ± 0.02

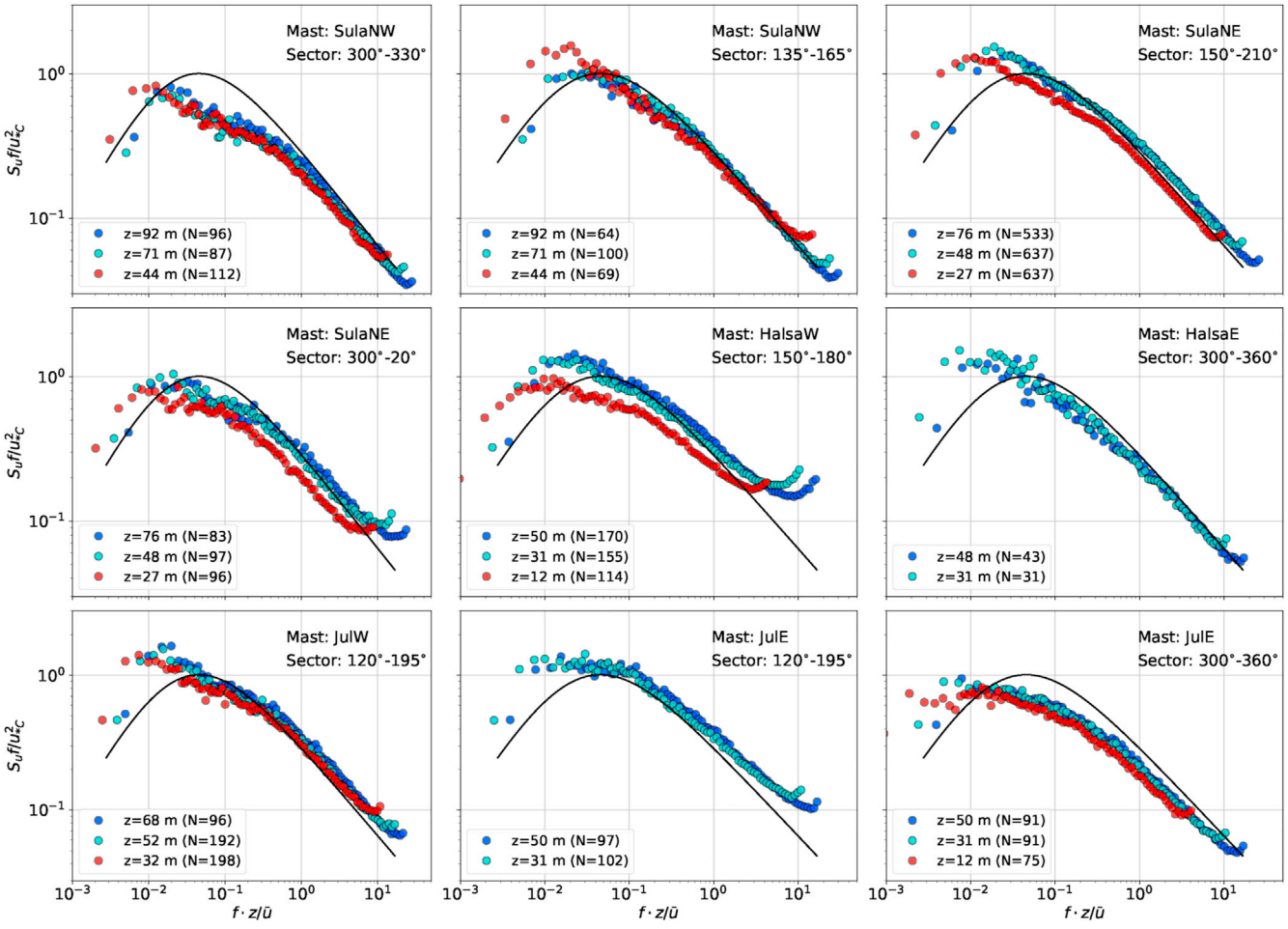

Fig. 2. Estimated along-wind velocity spectra for long-fetch winds in Sulafjorden, Halsafjorden and Julsundet, from 01-01-2018 to 31-12-2019. The solid line is the Kaimal spectrum (eq. (9)).

a Hanning window and two blocks with 50% overlapping. The use of multiple segments is needed to reduce the bias and the uncertainties associated with the modified periodogram estimate. However, increasing the number of segments reduces also the frequency resolution and increases the lowest frequency recorded. In the present case, two overlapping segments were found to be a reasonable trade-off. The use of 50% overlapping is advised by Carter et al. (1973) when a Hanning window is considered. The velocity spectra are ensemble-averaged using arithmetic median for the analysed period and were further smoothed by using bin-averaging over logarithmically-spaced bins, which has the advantage to affect the high-frequency range only. Smoothing filters which distort the low-frequency range of the spectrum, such as the Savitzky-Golay filter (Savitzky and Golay, 1964), may not be adapted for such a purpose.

The co-coherence was estimated using Welch's algorithm with ten overlapping segments to smooth the estimates. A larger number of segments than for the one-point spectra is required because the two-point cross-spectrum displays a larger bias and random error. Before computing the co-coherence, the time series were decimated down to 2 Hz to speed-up the algorithm. Also, for the range of vertical separations considered, the co-coherence is nearly zero at frequencies above 1 Hz. The decimation was done after application of a low-pass Chebyshev IIR filter of order eight to reduce aliasing. The estimation of the vertical co-coherence on a single met-mast requires that the data on each sensor passes the data quality assessment described in Midjiyawa et al. (2021). This further reduces the amount of data available for the analysis of the co-coherence.

5. Results

5.1. Velocity spectra

The one-point spectra were studied following the wind sectors classification by Midjiyawa et al. (2021). The sectors are named long-fetch winds and short-fetch winds as described in section 1. For the sake of clarity, the classification is reproduced in Tables 3 and 4 along with their corresponding integral flow characteristics estimated by the anemometer located closest to 50 m above ground.

Using surface-layer scaling, the spectra are normalized by the square of the friction velocity u_{*C} (where c stands for the classical method in eq. (5)). Figs. 2–4 and Figs. 5–7 display the velocity spectra for long-fetch winds and short-fetch winds, respectively. The figures are separated with respect to the three wind components u, v and w. Sectors with less than ten samples were dismissed as they may be associated with statistical uncertainties too large to be meaningful.

5.1.1. Low-frequency part of the velocity spectra

The dynamic wind-induced response of long-span bridges is governed by the low-frequency turbulent wind fluctuations. The planned bridges crossings at Julsundet, Halsafjorden and Sulafjorden will likely have their dominant eigenfrequencies between 0.02 Hz and 0.20 Hz, i.e. possibly lower than those from the longest suspension bridges in the world (Fujino, 2018). To adequately design such bridges, the large uncertainties associated with the lower-frequency region of the velocity

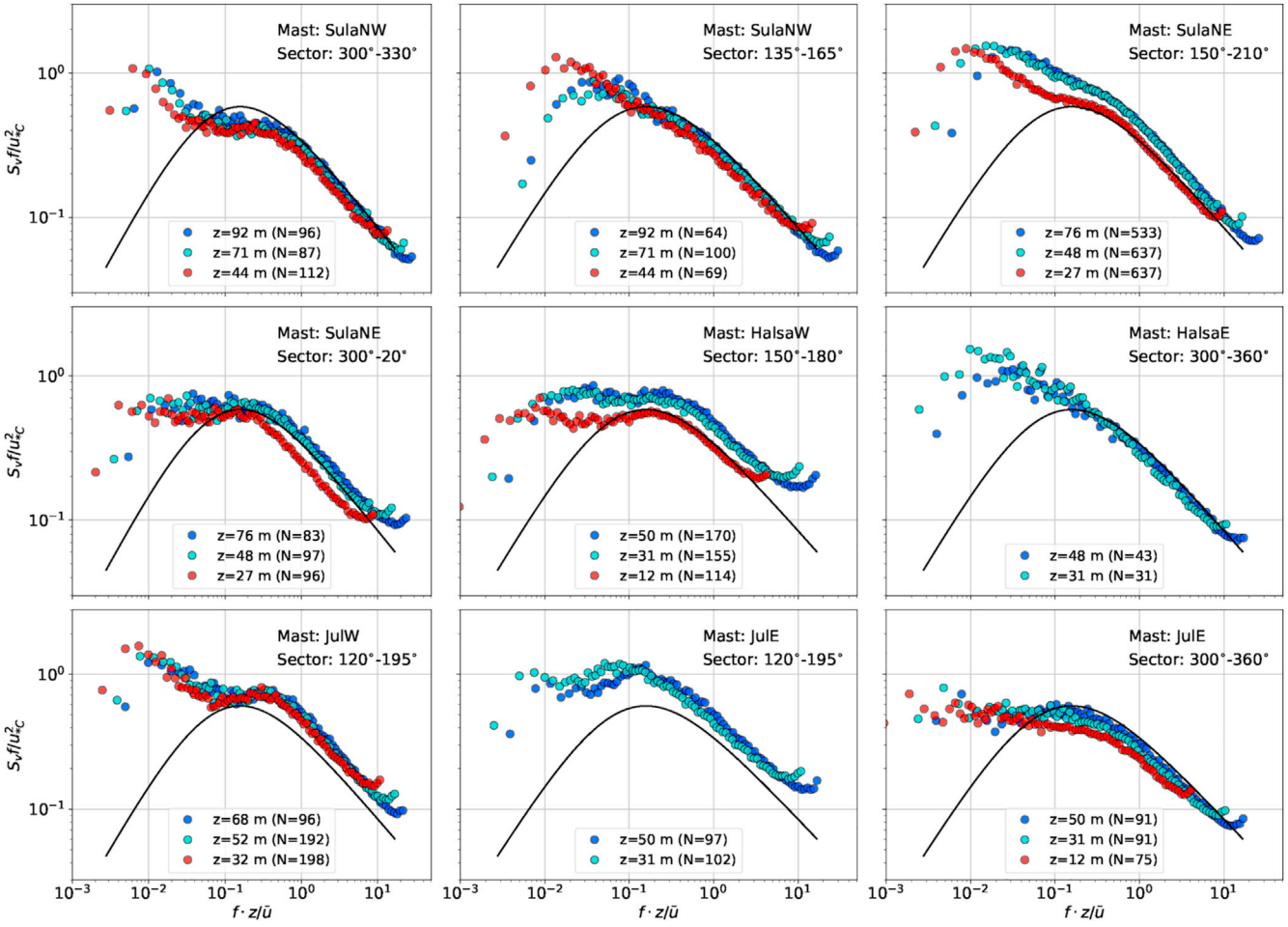

Fig. 3. Estimated cross-wind velocity spectra for long-fetch winds in Sulafjorden, Halsafjorden and Julsundet, from 01-01-2018 to 31-12-2019. The solid line is the Kaimal spectrum (eq. (10)).

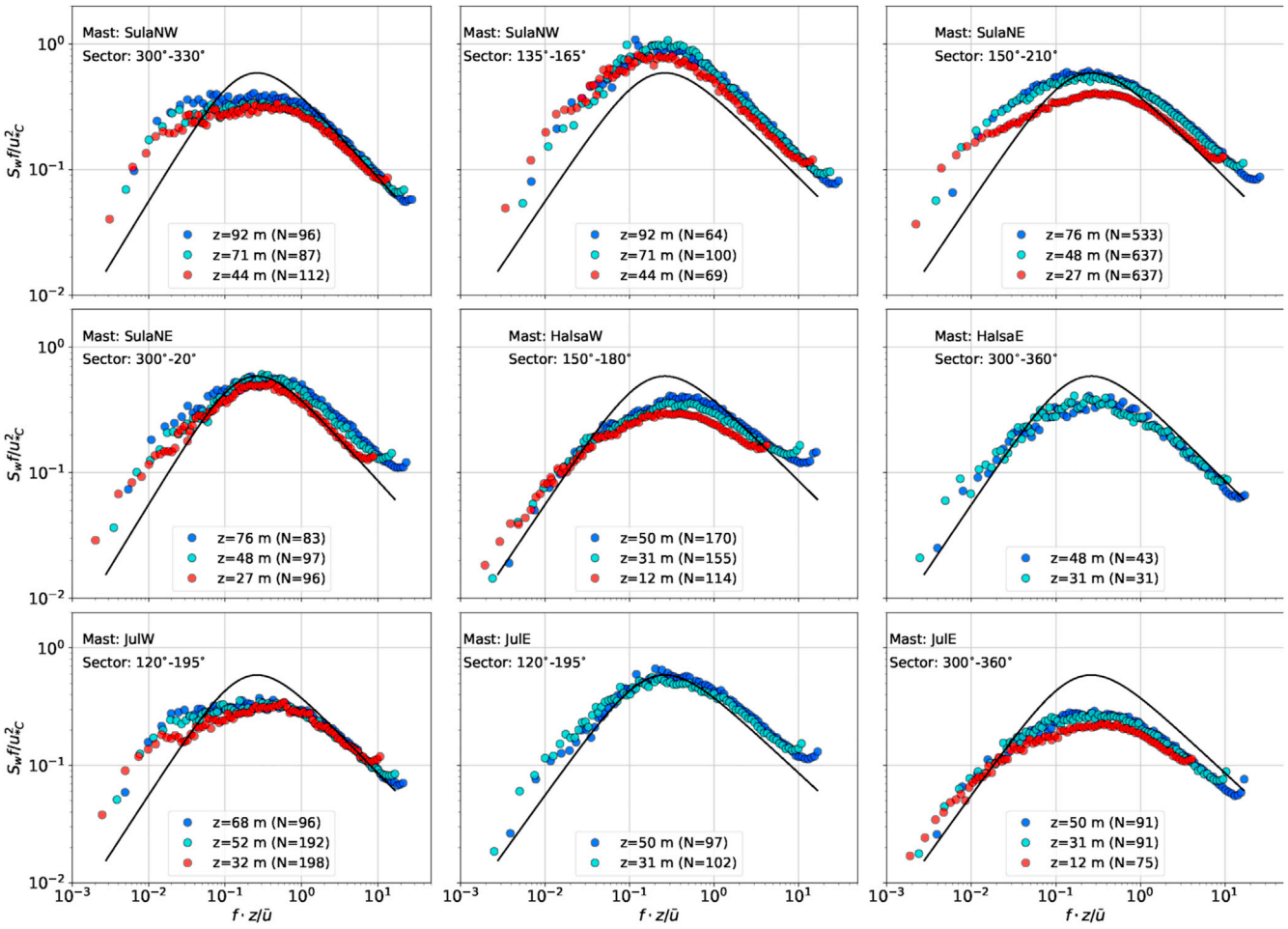

Fig. 4. Estimated vertical velocity spectra for long-fetch winds in Sulafjorden, Halsafjorden and Julsundet, from 01-01-2018 to 31-12-2019. The solid line is the Kaimal spectrum (eq. (11)).

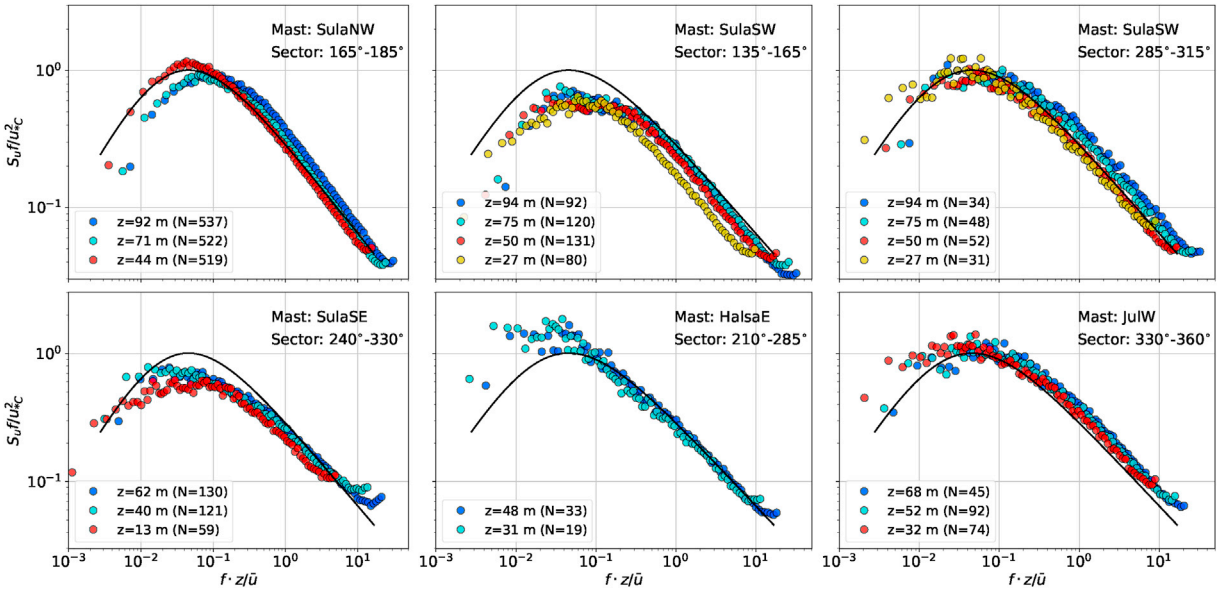

Fig. 5. Estimated along-wind velocity spectra for short-fetch winds in Sulafjorden, Halsafjorden and Julsundet, from 01-01-2018 to 31-12-2019. The solid line is the Kaimal spectrum (eq. (9)).

spectra need to be reduced. These uncertainties can be addressed using a probabilistic approach (e.g. Fenerci and Øiseth, 2018; Solari and Piccardo, 2001) or a more physical approach, which relies on a classification of the topography upstream of the measurement location

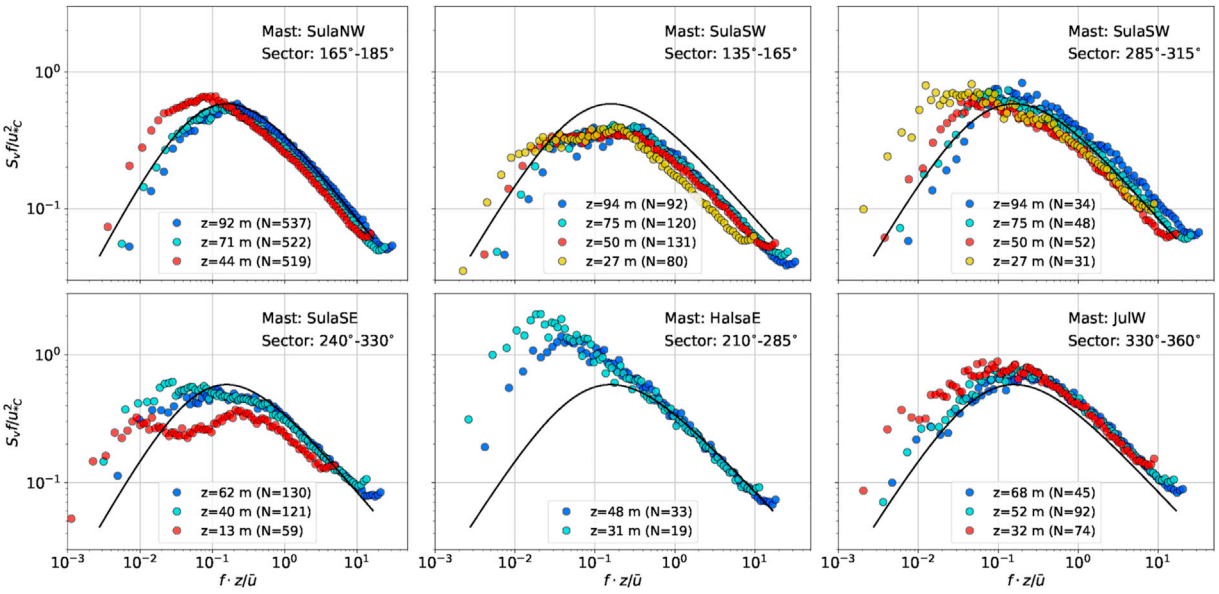

Fig. 6. Estimated cross-wind velocity spectra for short-fetch winds in Sulafjorden, Halsafjorden and Julsundet, from 01 to 01–2018 to 31-12-2019. The solid line is the Kaimal spectrum (eq. (10)).

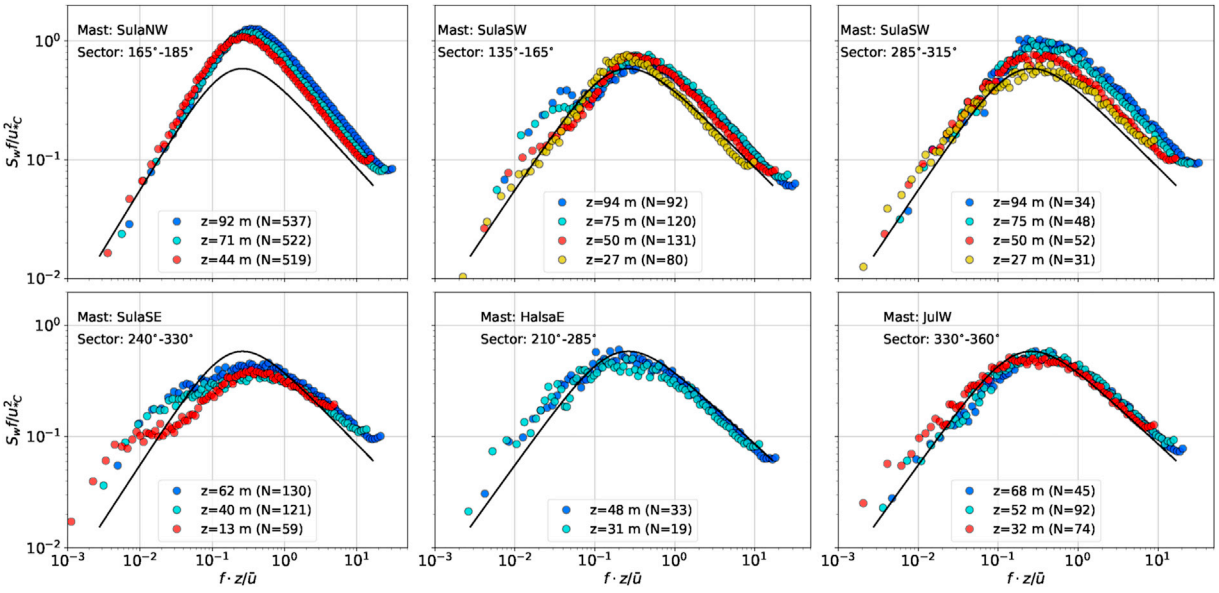

Fig. 7. Estimated vertical velocity spectra for short-fetch winds in Sulafjorden, Halsafjorden and Julsundet, from 01-01-2018 to 31-12-2019. The solid line is the Kaimal spectrum (eq. (11)).

combined with a rigorous data-quality assessment. The latter method is adopted hereafter since the dataset gives a unique possibility to identify analogous flow characteristics within three different fjords.

The low-frequency spectral content of S_u and S_v, estimated for long-fetch winds, is larger than predicted by the Kaimal model. Furthermore, the spectral peak is moved to the spectrum's lower frequency part. This can be seen, for example, in SulaNW (sector 300°-330°), HalsaE (sector 300°-360°), and JulE (sector 300°-360°). This feature, observed for multiple masts in the selected fjords (Figs. 2 and 3) may be one shared spectral characteristic associated with long upstream fjord fetch. On the other hand, for short-fetch winds (Figs. 5 and 6) they agree fairly well with the Kaimal spectrum.

The horizontal spectra estimated in SulaNW (sector 135°-165°) and SulaNE (sector 300°-20°) show spectral characteristics compatible with long-fetch winds. However, the calculated integral flow characteristics displayed in Table 3 suggest otherwise. The turbulence intensity for both masts and sectors is approximately 0.13 ± 0.03, whereas the normalized standard deviations σ_w/u_* are 1.97 ± 0.34 and 1.71 ± 0.30, respectively. These values are characteristics typically observed for short-fetch winds. The inconsistency between integral and spectral flow characteristics indicates that there might be a localized flow from a secondary valley which influences the integral turbulence characteristics (Cheynet et al., 2020). Therefore, further investigation may be required using wind tunnel tests or CFD flow simulation.

The vertical spectra S_w reasonably follow surface-layer scaling as they superpose on each other at $f_r < 0.1$. However, the normalized S_w spectra are above the Kaimal model. This is valid for both long-fetch and short-fetch winds (Figs. 4 and 7) except for at SulaSE (sector 240°-330°) and SulaSW (sector 135°-165°). The spectral peak of the vertical velocity component is located at higher frequencies than the horizontal

components, which reflects the fact that eddies are generally smaller for the w component than for the u and v components (Busch and Panofsky, 1968; Panofsky et al., 1982; Højstrup, 1981). Smaller eddies, located at high wavenumbers, are less affected by the local topography than larger eddies, which may explain why surface-layer scaling seems to apply better to this component.

The low-frequency spectral peak of the horizontal components seen in long-fetch winds, which is more pronounced as the measurement height decreases, was previously observed in coastal areas for a wind coming from the sea (Yu et al., 2008), but also in the offshore environment (Cheynet et al., 2018). This is likely because S_u and S_v, especially at low frequencies, do not follow MOST (Kaimal et al., 1972). For short-fetch winds, the low-frequency part of the spectrum has a lower spectral energy content than for long-fetch winds. The difference indicates that, although large eddies characterized by low wavenumber could be modified by blocking by the ground, the sea surface or hills (Frank, 1996), the irregular topography may break down the large eddies and, therefore, filter out the low-frequency fluctuations.

For long-fetch winds, the PSD estimates display a double peak, particularly apparent in the cross-wind component (Fig. 3). This is the case for SulaNW (sector 300°-330°), SulaNE (sectors 300°-20° and 150°-210°), HalsaW (sector 150°-180°), JulW (sector 120°-195°) and JulE (sectors 120°-195° and 300°-360°). A broad spectral peak, which sometimes looks like a plateau, has also been reported by Drobinski et al. (2004). For short-fetch winds (Figs. 6 and 7), only the sector 240°-330° at SulaSE has a more pronounced spectral plateau for the vertical velocity component and a double peak for the cross-wind component.

Furthermore, the cross-wind spectra for JulW (sector 120°-195°) and SulaNW (sector 300°-330°) both show the two most pronounced double peaks. These mast locations and associated wind direction are characterised by wind travelling along the shoreline with mountainous topography on one side and the water inlet on the other. These low-frequency peaks may be due to sub-meso fluctuations. However, it is unsure whether these fluctuations come from topographic elements since similar peaks were observed in an offshore environment for the cross-wind component (Cheynet et al., 2018).

The presence of the spectral plateau may not be limited to the lower part of the surface layer, where blocking by the surface is dominant (Drobinski et al., 2004). Strong shear may also be responsible for a wider spectral peak than predicted in the surface layer, especially for the vertical component (Drobinski et al., 2004). The spectral plateau, when visible, is characterized by $fS_v/u_*^2 \approx 1$ (Högström et al., 2002). The aforementioned double peak and spectral plateau are less distinguishable for short-fetch winds which suggest that high-roughness does not seem to favour the distortion of the eddies by the ground but rather act as a high-pass filter.

The semi-empirical models commonly found in the literature (Kaimal and Finnigan, 1994; Tieleman, 1995; von Kármán, 1948) rarely account for the presence of a spectral plateau or a double peak. If the von Kármán spectral model (von Kármán, 1948) is used, the estimation of the integral length scale is generally required. This can be done using the low-frequency range of the velocity spectrum or the spectral peak, which is not always clearly defined. Therefore, the absence of a peak or the presence of multiple peaks can lead to significant errors in the estimation of the integral length scales (Iyengar and Farell, 2001; Cheynet et al., 2018; Panosfsky and Dutton, 1984).

5.1.2. High-frequency part of the velocity spectra

The high-frequency range of the velocity spectra is defined as $f_r > 2$ in the following. This range is of lesser importance for the computation of the dynamic displacement of a long-span bridge. However, it is essential to have some confidence in the estimation of the turbulence characteristics. The high-frequency range of the velocity spectrum is characterized by small eddies, which are less affected by the topography. Under neutral conditions, in the surface layer, which are the conditions relevant for structural design, the velocity spectra normalized by f/u_*^2 are expected to satisfy eqs. (1) and (2). A further quality assessment can be done by comparing the ratios S_w/S_u which should converge toward 4/3 in the inertial subrange (Kolmogorov, 1941; Kaimal et al., 1972). Deviations from these asymptotic relations can be linked to flow-distortion issues, aliasing, nonphysical signal, strong thermal stratification, improper data processing or inadequate method for PSD estimations. Failure to identify the ratio S_w/S_u at high reduced frequencies can lead to a considerable increase of the measurements uncertainties. In this regard, the exploration of the high-frequency part of the velocity spectra offers relevant information on the data quality.

For both long-fetch and short-fetch winds, the normalized S_u and S_v are superposed with each other at $f_r > 2$, except for a limited number of cases e.g SulaNW and the lowest anemometers at the other masts as they may be affected by flow distortion from the surrounding trees. The estimated S_w spectra, in both long-fetch and short-fetch winds, are superposed with each other, as seen for example at JulW (sector 330°-360°) for short-fetch winds and at HalsaE (sector 300°-360°) for long-fetch winds. However, the S_w spectra do not always follow the Kaimal model at higher frequency with the only exception at HalsaE (sector 210°-285°), characterized as short-fetch winds.

The only met-mast in which a consistent collapse is observed with the Kaimal spectrum at a higher frequency for every velocity component is HalsaE, for the sectors 300°-360° and 210°-285°, characterized as long-fetch winds and short-fetch winds, respectively. The HalsaE mast is located in Halsafjorden, where measurements are less influenced by the topography than in the other two fjords (Midjiyawa et al., 2021). In JulW (sector 120°-195°), characterized as long-fetch winds, the S_w spectrum agrees well with the Kaimal model at high reduced frequencies, whereas it is not the case for the horizontal components.

Following surface-layer scaling, using the friction velocity and the measurement height as the scaling velocity and length, the spectra are expected to superpose onto each other. In this study, S_u, S_v and S_w show the adequacy of surface layer scaling at higher frequency in fjord-like topography. On the other hand, systematic discrepancies with the Kaimal spectrum at high frequencies may indicate that the local friction velocity u_* is biased. The investigation of the alternative methods of computing u_* is done in section 5.2.

5.1.3. Influence of topography on the auto- and cross-spectra

The real part of the cross-spectrum, which is called co-spectrum, and its imaginary part, named quad-spectrum herein, are studied for all met-masts and all elevations. For the sake of brevity, Fig. 8 shows the normalized cross-spectrum for only two distinctive cases. The mast locations and sectors that are chosen for illustrative purpose are SulaNW for the sector 165°-185° and HalsaW for the sector 285°-360°. The quad-spectrum reflects the blocking by the ground (Mann, 1994). Therefore, the absolute value of the quad-spectrum should decrease with altitude. However, it is not always the case for the fjords analysed, where the quad-spectrum sometimes increases with height. This increase could be related to the fact that the terrain upstream of the masts is often heterogeneous. For long-fetch winds, the quad-spectra and co-spectra have similar amplitudes for all the met-masts analysed. This suggests that even for long-fetch winds, the blocking by the ground or the mountain slopes is not negligible. In many cases, the quad-spectrum estimates are substantially larger in absolute value than reported offshore (e.g. Cheynet, 2018). Flow distortion by a canopy, defined as the vegetation cover above ground, is sometimes visible in the velocity data recorded at heights around or below 30 m above the ground, as shown in Fig. 9 for HalsaE (sector 150°-180°). The south side of HalsaE is dominated by a long fetch. The velocity spectrum at 31 m above the ground shows a narrow peak near $f_r \approx 0.5$, likely, reflecting distortion of the flow by a canopy, as previously observed by e.g. Dellwik et al. (2014).

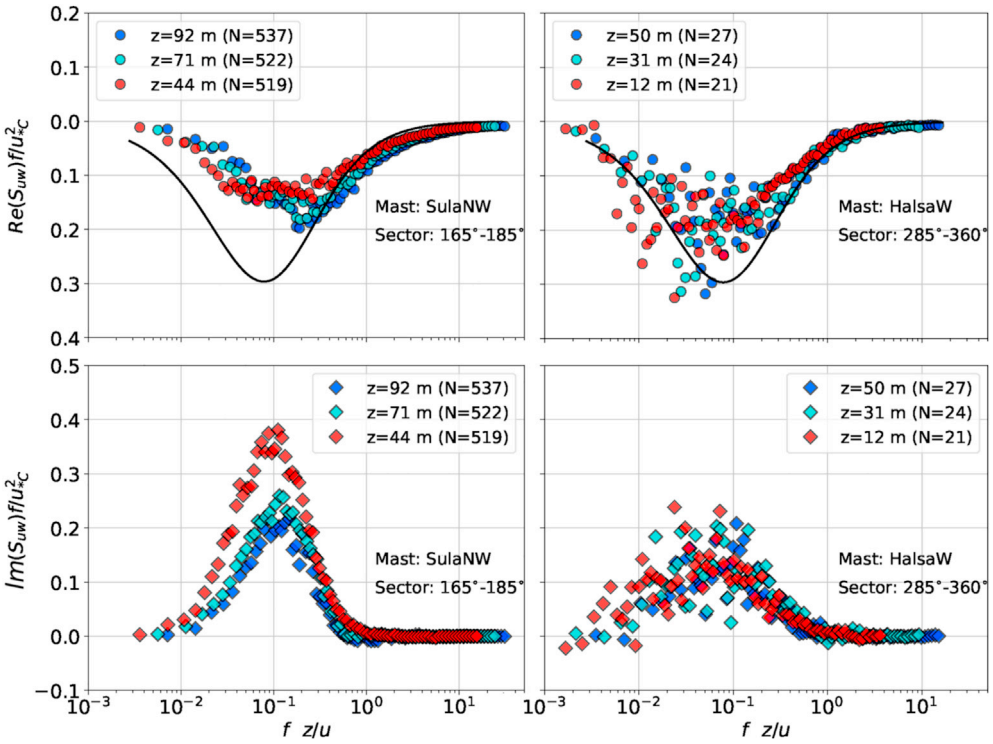

Fig. 8. Normalized real and imaginary parts of the cross-spectrum S_{uw} estimated using the records from SulaNW and HalsaW from 01-01-2018 to 31-12-2019. The black line is the Kaimal model given in eq. (12).

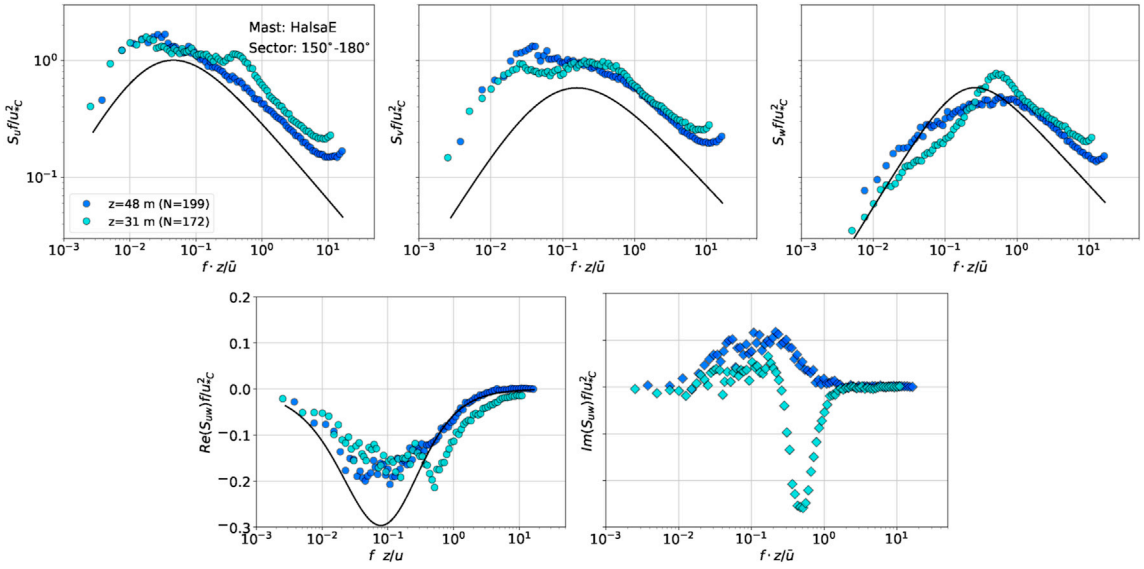

Fig. 9. Canopy-induced flow distortion at $z = 31$ m is visible in the velocity spectra estimated at HalsaE (sector 150°-180°) between 01-01-2018 to 31-12-2019. The black lines are the Kaimal model (eq. (9) and (12)).

5.1.4. Spectral ratios

The spectral ratios between the vertical and along wind components are shown for some of the masts in Fig. 10. For the sake of brevity, only three representative masts are selected due to the similarity of the findings. The resulting ratios can be classified into three groups as illustrated in Table 5. The first group is the one in which S_w/S_u converges steadily towards 4/3. This is the case for HalsaE (sector 300°-360°) where the 4/3 value is reached at $f_r \geq 3$, which is consistent with Kaimal et al. (1972). The second is the group where the ratio is significantly higher than 4/3 at $f_r > 1$, which is the case for SulaNW (sector 165°-185°). For this sector, the three anemometers show similar ratios, which suggests that the observation is not related to an instrumental error. Yet, such a value is abnormally large, which might be linked to the presence of a hill upstream of the mast responsible for a large negative angle of attack, as indicated by Midjiyawa et al. (2021). For large negative incidence angles, flow separation may occur. In this situation, the vertical and along-wind components cannot be reliably retrieved using the double rotation technique.

The third group is the one in which the ratio S_w/S_u remains below 4/3, as observed for HalsaW (sector 150°-180°). Both flow distortion and aliasing can be responsible for such behaviour. In the present case, the three anemometers display a similar trend for S_w/S_u, indicating that flow

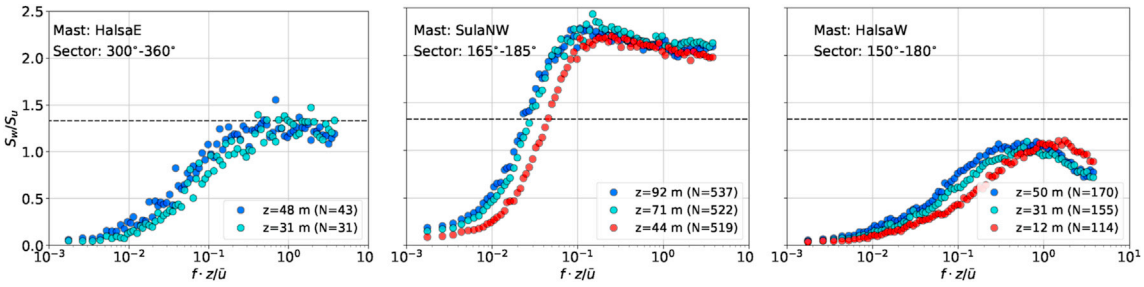

Fig. 10. Spectral ratio S_w/S_u at SulaNW (sector 165°-185°), HalsaW (sector 150°-180°), and HalsaE (sector 300°-360°) from 01-01-2018 to 31-12-2019. The black dashed line is 4/3, which is a value representative of the local isotropy in the inertial subrange.

Table 5
Classification of the result obtained in spectral ratio calculation at $f_r \geq 3$; Group– I $S_w/S_u \frac{4}{3}$, Group– II $S_w/S_u > \frac{4}{3}$, Group– III $S_w/S_u < \frac{4}{3}$

Mast name	Sector	Group categories
SulaNW	135–165	II
	165–185	II
	300–330	II
SulaNE	300–20	II
	150–210	II
SulaSW	135–165	II
	285–315	II
	315–345	I
SulaSE	240–330	I
HalsaW	150–180	III
	285–360	I
HalsaE	150–180	III
	210–285	I
	300–360	I
JulWest	120–195	III
	330–360	I
JulEast	120–195	III
	210–285	I
	300–360	III

distortion by the surrounding vegetation is unlikely to explain the failure of S_w/S_u to converge toward 4/3. Fig. 2 shows that aliasing is more important for the u component than for the w component. Therefore, the presence of aliasing is reflected by the negative slope of S_w/S_u at $f_r > 1$ as seen in the right panel of Fig. 10. Without aliasing, the ratio would likely have converged toward 4/3.

5.2. Reassessment of the friction velocity as a scaling velocity

Some of the PSDs estimates are systematically above the Kaimal spectra, suggesting that the friction velocity used is underestimated. The underestimation cannot be corrected by using the surface friction velocity. Firstly, because the reduction of the friction velocity from the surface to the measurement height is unlikely to be large enough to explain the discrepancies observed. Secondly, because the terrain is heterogeneous, such that the friction velocity at the surface is not representative of the same roughness as at the anemometer position. Therefore, in this situation, extrapolation techniques are not recommended. The adequacy of the local friction velocity u_* as scaling velocity is investigated by estimating it with the three different methods summarised in eqs. (5), (6) and (8). The dataset from JulE (sector 210°-285°) is selected for velocity spectra indicating a possible bias in the estimation of u_*. The western side of JulE is characterized by a long fjord fetch, the length of which is the width of Julsundet. For this sector, the PSDs of the velocity fluctuations showed characteristics from long-fjord fetch but the imaginary part of the cross-wind spectra showed that the blocking by the ground or the surrounding hills was not negligible.

Fig. 11 shows that the influence of the method to compute u_* on the amplitude of the spectra is significant. The method by Klipp (eq. (6)) does not show a clear difference with the classical method (eq. (5)). The application of eq. (8), on the other hand, leads to PSD estimates that satisfy eqs. (1) and (2) by superposing onto each other and with the Kaimal model at high frequencies. One exception is the S_w spectrum estimated using the data collected by the anemometer located at 12 m above the ground. These measurements are suspected to be influenced by the trees or the vegetation around the mast, as stated in Furevik et al.

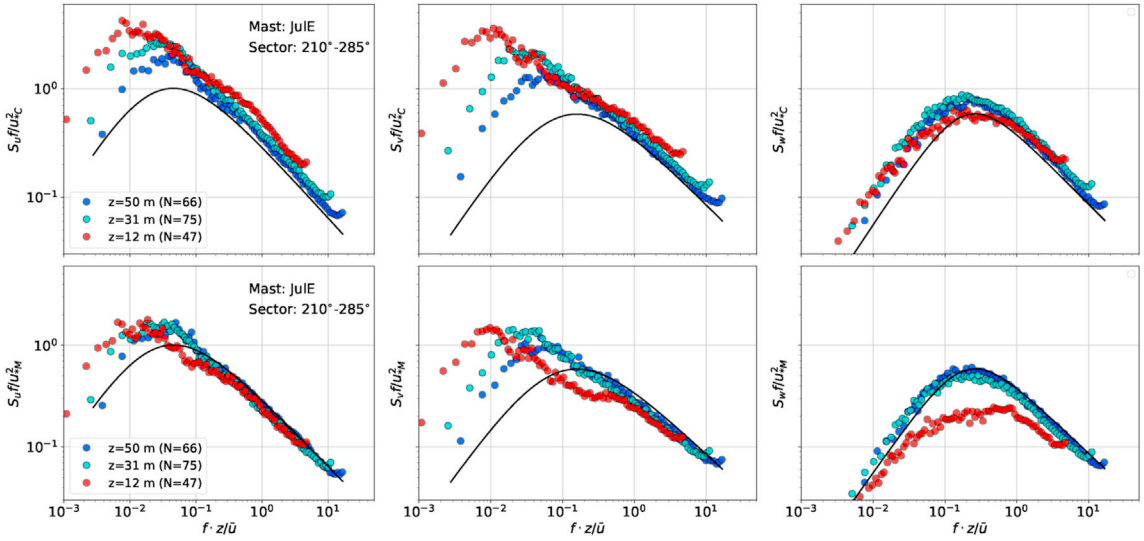

Fig. 11. Along-wind, cross-wind, and vertical velocity spectra estimated at JulE (sector 210°-285°) for the period from 01-01-2018 to 31-12-2019. Top panel: the spectra are normalized by eq. (5). Bottom panel: the spectra are normalized by eq. (8). The black line is the Kaimal model given from eq. (9) to eq. (11).

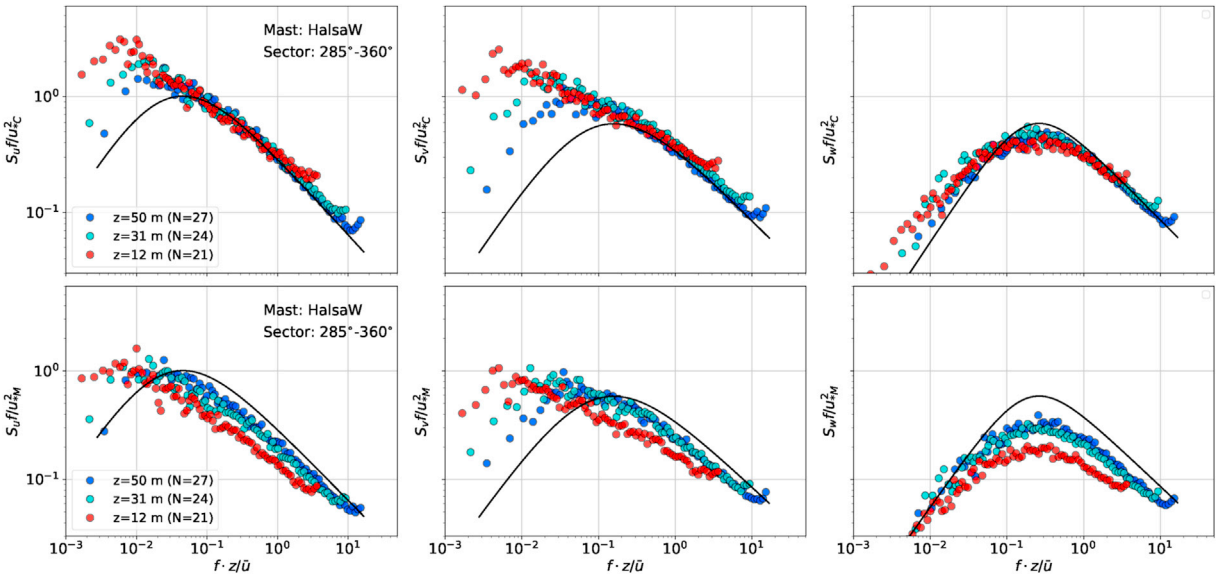

Fig. 12. Velocity spectra estimated at HalsaW (sector 285°-360°) for the period from 01-01-2018 to 31-12-2019. Top panel: the spectra are normalized by eq. (5). Bottom panel: the spectra are normalized by eq. (8). The black line is the Kaimal model given from eq. (9) to eq. (11).

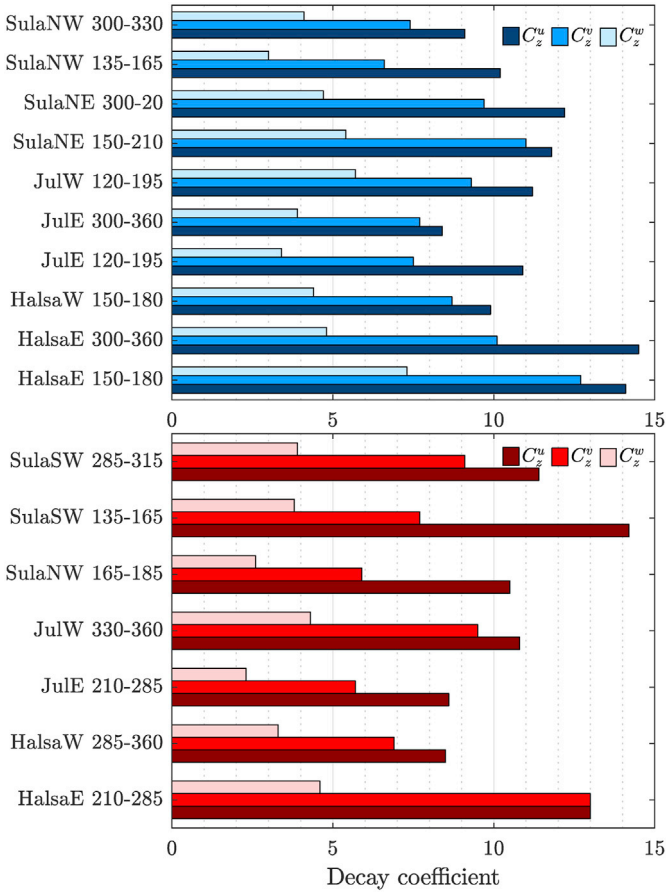

Fig. 13. Davenport decay coefficient at Sulafjorden, Halsafjorden and Julsundet, for long-fetch winds (top) and short-fetch winds (bottom).

(2020). The use of eq. (8) indicates that surface layer scaling may be applicable in a Norwegian fjord, providing that it is based on an adequate determination of the friction velocity used as a scaling parameter.

However, the application of eq. (8) does not always seem adequate as shown by Fig. 12. For the case at hand (HalsaW, sector 285°-360°), the underestimation of the friction velocity is less important than for JulE (sector 210°-285°). In addition, the use of eq. (5) seems already appropriate as shown by the good agreement between the S_w spectrum and the Kaimal model in the high-frequency range. Therefore, in this situation, the application of eq. (8) would not be recommended. Choosing the proper method to compute u_* cannot rely on the argument that the shear stress $\overline{u'v'}$ is non-negligible compared to $\overline{u'w'}$ only. One possible reason for the application of eq. (8) instead of eq. (5) might be the presence of a substantial horizontal mean wind shear, which is considerable in Sulafjorden or Julsundet compared to Halsafjorden (Midjiyawa et al., 2021). A further investigation of the turbulent shear stresses in terms of quadrant analysis (Shaw et al., 1983) might also help to identify situations where eq. (6) or eq. (8) would be preferred to eq. (5).

5.3. Co-coherence

5.3.1. Application of the davenport model

Fig. 13 displays the fitted decay coefficients for long-fetch and short-fetch winds. We remind the reader that the least-square fit is conducted by simultaneously considering every combination of measurement height. For long-fetch winds, the decay coefficients are found to vary as follow: $8.4 \leq C_z^u \leq 14.5$, $6.6 \leq C_z^v \leq 12.7$, and $3.0 \leq C_z^w \leq 7.3$. For short-fetch winds, the decay coefficient are similar as for long-fetch winds, with $8.5 \leq C_z^u \leq 14.2$, $5.7 \leq C_z^v \leq 13.0$, and $2.3 \leq C_z^w \leq 4.6$, respectively. The computed Davenport decay coefficients are similar for the two fetches considered. The range of values found is also similar to those found by Hui et al. (2009), who also focused on two distinctive sectors with different topographic characteristics.

The decay coefficients estimated at SulaNE for a northwesterly wind coming from the ocean are remarkably close to those obtained offshore by Cheynet et al. (2018), which were computed using similar altitudes and separations. This observation suggests that records obtained on the shore of a mountainous fjord open to the sea may, under certain conditions, exhibit flow characteristics similar to those observed in the offshore environment. The northwesterly wind is flowing past the mountainsides at SulaNW, which may explain why the decay coefficients estimated from this mast deviate from those obtained at SulaNE. The average values of the decay coefficients computed in Fig. 13 are also similar to those from the handbook N400 for bridge design in Norway (Norwegian Public Road Administration, 2015), which are $C_z^u = 10$, $C_z^v = 6.5$ and $C_z^w = 3$. However, the handbook N400 assumes that the decay

coefficients are identical for lateral and vertical separations, which may not be the case in reality, especially in complex terrain.

Probabilistic approaches have been proposed for several decades to account for the observed variability of the decay coefficients (e.g. Solari and Piccardo, 2001; Hoffmann et al., 2017). Fig. 13 show that the variation of the decay coefficient is not negligible for wind load calculation. However, this variability is lower than reported in the literature, given the large variety of fetch and locations included in the present study. Over the last sixty years, the large scatter of the reported decay coefficients can partly be explained by the different environmental and experimental conditions. For vertical separations, the Davenport decay coefficient is known to depend on the spatial separation (Kristensen et al., 1981), the measurement height (Bowen et al., 1983), the terrain roughness (Ropelewski et al., 1973) and the thermal stratification of the atmosphere (Soucy et al., 1982; Cheynet et al., 2018). Besides, the fitted decay coefficient can be biased, depending on the number of sensors used, the signal-to-noise ratio and the algorithm considered. Welch's method (Welch, 1967) is generally used to estimate the co-coherence. A crucial step for the application of this algorithm is the choice of the number of overlapping segments, which can significantly affect the value of the decay coefficient (Saranyasoontorn and Manuel, 2008; Mann, 1994). Finally, it should be noted that the present study focuses on the co-coherence, which captures the simultaneous fluctuations of velocity along a line. However, the decay coefficient is sometimes estimated using the magnitude-squared coherence, which contrary to the co-coherence, does not converge toward zero at high-frequencies because it is a biased estimate. Although probabilistic methods are certainly valuable to assess the variability of turbulence characteristics, they should be used with caution if the source of uncertainties is unclear.

In the present case, the variability of the decay coefficients is likely due to the different measurement heights, separation distances between the sensors and the heterogeneity of the terrain. For example, most of the decay coefficients are slightly larger in Halsafjorden and Julsundet than in Sulafjorden because the anemometers on JulE, JulW, HalsaW and HalsaE are closer to the surface than those in Sulafjorden. The increasing values of the decay coefficients as the measurement height decreases

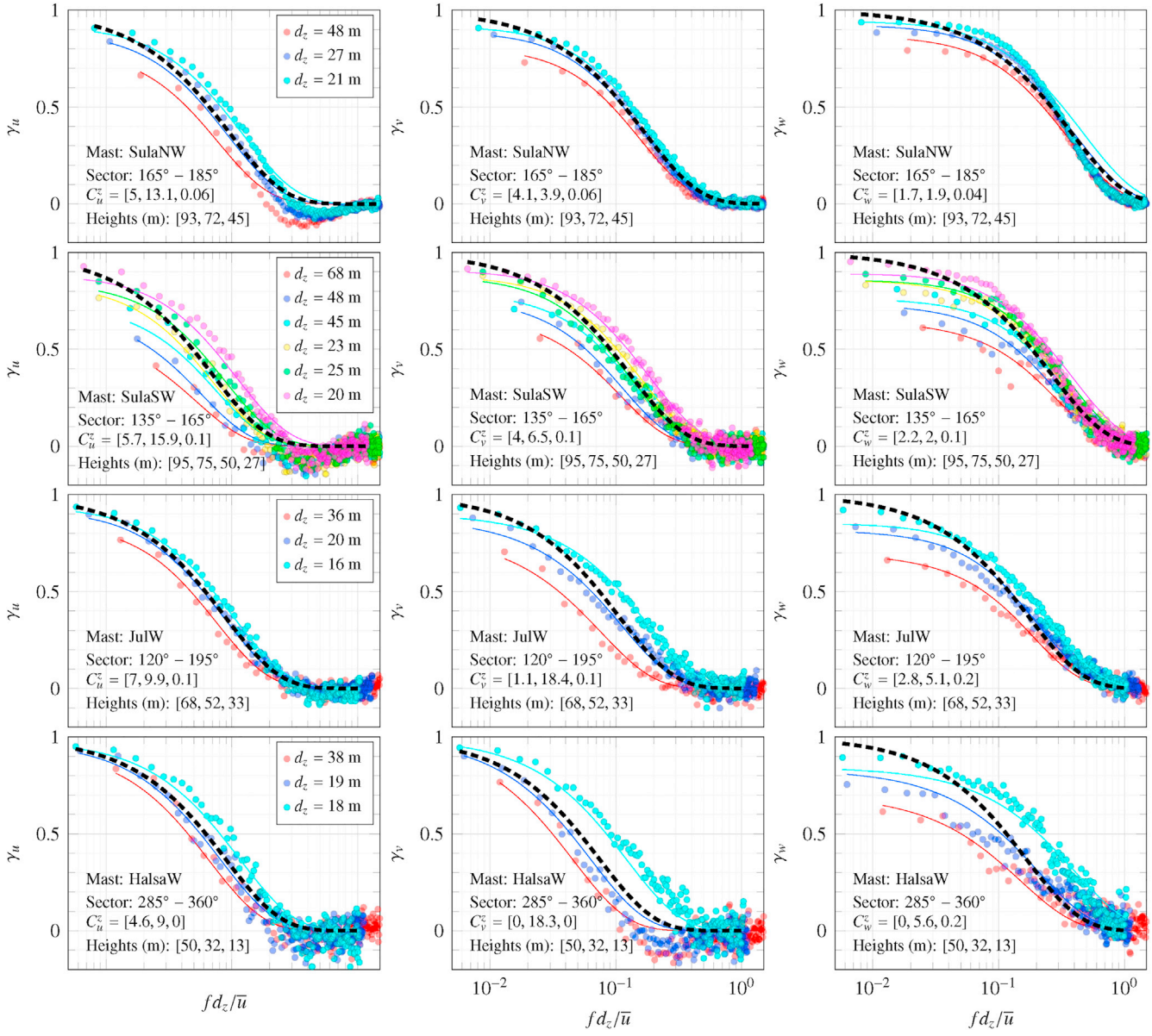

Fig. 14. Along-wind, cross-wind and vertical co-coherence for selected masts at Sulafjorden, Halsafjorden and Julsundet for the period from 0 to 31-12-2019. The continuous lines are the fitted modified Bowen coherence model and the thick dashed lines correspond the Davenport model. In this figure, the notation C_z^i corresponds to $C_z^i = [C_1^i, C_2^i, C_3^i]$ where $i = \{u, v, w\}$.

reflect the presence of smaller eddies close to the surface. A large mean wind shear may also increase the uncertainties associated with the estimated decay coefficient because the coherence is a turbulence characteristic that is meaningful only if the flow is fairly homogeneous. Nevertheless, the dependency of the decay coefficients on the mean wind speed u is likely small, as suggested by e.g. Schlez and Infield (1998), because the Davenport model accounts for the change of the coherence with u.

5.3.2. Application of alternative coherence models

Fig. 14 shows the co-coherence estimates for each mast and the wind sectors selected. The solid lines correspond to a least-square fit with eq. (19), which was referred to as the modified Bowen model. The dashed lines correspond to a least-square fit with the Davenport model.

Per definition, the Davenport coherence model reduces to a single curve when expressed as a function of fd_z/u which is called hereafter Davenport similarity. Although the application of eq. (19) leads to a much better modelling of the vertical co-coherence than the Davenport model, the parameters C_1^i and C_2^i show also a greater variability than the Davenport decay coefficients. A larger scatter is expected since a higher number of free parameters than in the Davenport model is used. A further reduction of the variability of these coefficients could be achieved by combining separations below 10 m and others close to 100 m, by increasing the number of sensors or assessing alternative fitting techniques. However, such investigations are out of the scope of the present study. In structural dynamics, the exponential decay function by Davenport (1961a) has the advantage of simplicity. This is likely the reason why it is adopted by EN 1991-1-4 (2005) and subsequently in the Norwegian Public Road Administration (2015) Handbook.

The modified Bowen model highlights the limits of the Davenport model to describe the variation of the decay coefficient with vertical separations. If a floating-bridge with pontoons is constructed in Sulafjorden, the proximity of the girder with the sea surface may require a reassessment of the Davenport model to adequately capture the spatial correlation of turbulence. A similar reassessment may be required for the bridge towers, which will be slender structures as high as 200 m (Wang et al., 2018). They will be particularly sensitive to turbulent effects during the construction phase (e.g. Ogawa et al., 1990; Wardlaw, 1990; Larose et al., 1998). A preliminary comparison between the Davenport coherence model and the modified Bowen model was conducted for a vertical cantilever beam in Cheynet (2018). The computation of the joint-acceptance functions, which quantifies the contribution of the co-coherence on the modal load, suggested that the Davenport model might lead to an overestimation of the turbulent load for the lowest modes of vibrations. A more detailed comparison for fjord-crossing bridges is, however, a topic for future work.

6. Conclusions

The present work complements the investigations carried out in Part-I, which assessed the integral flow characteristics. Here, we explored the spectral characteristics of turbulence to highlight the challenges and potential of wind measurements using met-masts located on the shoreline of the fjords. The understanding of these flow characteristics will help to identify spectral turbulence models suitable for wind engineering applications in mountainous terrain. Two years of continuous wind measurements on eight masts were analysed, at heights between 12 m and 95 m above ground. The study focused on wind speeds relevant to turbulence-induced load in the context of bridge design, i.e. stationary wind conditions with mean wind speed $u > 12\ \mathrm{m\,s^{-1}}$. The influence of the local topography on turbulence was assessed in the frequency space, which led to the following findings:

- The power spectral densities (PSDs) of the along-wind and cross-wind components, denoted S_u and S_v, respectively, displayed a higher amplitude at low frequencies for long-fetch wind compared to the short-fetch cases. In contrast, the PSD estimate S_w of the vertical component did not show any significant influence of the fetch on their low-frequency range. However, the S_w spectra, estimated in some met-masts and for some specific sectors, have a much higher spectral peak compared to the Kaimal model. The velocity spectra estimated for long-fetch wind often showed a double spectral peak and a spectral plateau.
- The ratio S_w/S_u reaches the theoretical value 4/3 on the mast HalsaE for the sector 300°-360° only. This mast is located in relatively flat terrain, as seen in Part - I of this study. In some cases, the spectral ratios suggest that high roughness moves the frequency at which local isotropy is reached beyond the highest frequency resolvable by the anemometers. In several situations, aliasing, which was highlighted in the PSD estimates, prevented the ratio S_w/S_u from converging toward 4/3.
- The quad-spectrum Im (S_{uw}) and the co-spectrum Re (S_{uw}) were often similar in magnitude, which highlighted the possible blocking by the ground and/or by the mountain slopes. In flat terrain or offshore, Im (S_{uw}) is generally much smaller than Re(S_{uw}), especially when the height increases. For engineering practices, studying the quad-spectrum could be useful to complement the traditional terrain classification by the roughness length.
- The friction velocity u_* was computed using three different methods. The goal was to identify which one was adequate in complex terrain, assuming that surface-layer scaling is applicable in Norwegian fjords. Some of the normalized PSD estimates, for example on JulE (sector 210°-285°), showed a deviation from surface-layer scaling, which was attributed to biased values of u_*. In this case, the application of Klipp's method was not conclusive. However, in some cases, the use of the norm of all the off-diagonal components of the Reynolds stress tensors led to normalized PSDs that satisfied surface-layer scaling, at least in the higher-frequency range. Further work is required to identify which method to compute the friction velocity is best suited, depending on the terrain features.
- The study of the vertical coherence of turbulence indicated that the Davenport decay coefficient did not depend significantly on the upstream topography. Depending on the sector selected, the averaged values of these decay coefficients are consistent with the N400 handbook (Norwegian Public Road Administration, 2015) and from the offshore platform FINO1 (Cheynet et al., 2018).
- The co-coherence estimates on the same met-mast rarely collapse into a single curve when expressed as a function of fd_z/u, contrary to what is predicted by the Davenport model. The application of coherence models derived from Bowen et al. (1983) and Cheynet (2018) highlighted the dependency of the coherence on dz and dz^2/z (z is the height above the ground and dz is the separation distance). Therefore, a more detailed assessment of the dependency of the Davenport decay coefficient on the separation and measurement height may be required in mountainous terrain.

The study by Midjiyawa et al. (2021) showed that the integral turbulent characteristics estimated on the shores of fjords may not be easily extrapolated on their middle part. The present study elaborates and complements the findings in Midjiyawa et al. (2021). Through a spectral analysis, we showed that the differences between the integral turbulence characteristics in fjords and in flat terrain were largely due to the low-frequency fluctuations. More importantly, the high-frequency range of the velocity spectra was found to be compatible with the model by Kaimal et al. (1972), which is advantageous for modelling purposes. Besides, the deployment of masts on the shores is also valuable for the safe design of bridges towers, which will be located close-by. The computation of the mean flow characteristics from multiple masts on the seaside is also meaningful for the validation of CFD models (Cheynet et al., 2020), which can be used to assess the wind conditions across the

fjord. The combined use of met-mast measurements and numerical analysis can further be complemented by remote sensing of wind and/or wind tunnel tests.

The present study indicates that if the fjords are crossed by single-span suspension bridges or floating suspension bridges, the turbulent wind loading on the main span may be properly modelled using the Simiu & Scanlan model (Simiu and Scanlan, 1996) and the Davenport model with the decay coefficients from the N400 handbook. If a floating pontoon bridge is constructed, the blocking by the sea surface may substantially affect the structure of turbulence and will therefore require a more in-depth investigation.

CRediT authorship contribution statement

Zakari Midjiyawa: Conceptualization, Methodology, Software, Validation, Formal analysis, Investigation, Data curation, Writing – original draft, Writing – review & editing, Visualization. **Etienne Cheynet:** Conceptualization, Methodology, Software, Validation, Formal analysis, Investigation, Supervision, Writing – original draft, Writing – review & editing. **Joachim Reuder:** Conceptualization, Supervision, Writing – review & editing. **Hálfdán Ágústsson:** Writing – review & editing. **Trond Kvamsdal:** Supervision, Project administration, Writing – review & editing.

Declaration of competing interest

The authors declare that they have no known competing financial interests or personal relationships that could have appeared to influence the work reported in this paper.

Acknowledgements

This work and the measurement campaign is financed by the Norwegian Public Roads Administration as part of the Coastal Highway E39 project in Mid-Norway. We also want to thank Birgitte R. Furevik and Jørn Kristiansen (Norwegian Meteorological Institute) for providing resources and guidance necessary for this work.

References

Bowen, A.J., Flay, R.G., Panofsky, H.A., 1983. Vertical coherence and phase delay between wind components in strong winds below 20 m. Boundary-Layer Meteorol. 26, 313–324. https://doi.org/10.1007/BF00119530.

Busch, N.E., Panofsky, H.A., 1968. Recent spectra of atmospheric turbulence. Q. J. R. Meteorol. Soc. 94, 132–148. https://doi.org/10.1002/qj.49709440003.

Carter, G., Knapp, C., Nuttall, A., 1973. Estimation of the magnitude-squared coherence function via overlapped fast fourier transform processing. IEEE Trans. Audio Electroacoust. 21, 337–344. https://doi.org/10.1109/TAU.1973.1162496.

Chamecki, M., Dias, N., 2004. The local isotropy hypothesis and the turbulent kinetic energy dissipation rate in the atmospheric surface layer. Q. J. R. Meteorol. Soc. 130, 2733–2752. https://doi.org/10.1256/qj.03.155.

Cheynet, E., 2018. Influence of the measurement height on the vertical coherence of natural wind. In: Conference of the Italian Association for Wind Engineering. Springer, pp. 207–221. https://doi.org/10.1007/978-3-030-12815-9_17.

Cheynet, E., Jakobsen, J.B., Reuder, J., 2018. Velocity spectra and coherence estimates in the marine atmospheric boundary layer. Boundary-Layer Meteorol. 169, 429–460. https://doi.org/10.1007/s10546-018-0382-2.

Cheynet, E., Jakobsen, J.B., Snæbjörnsson, J., 2016. Buffeting response of a suspension bridge in complex terrain. Eng. Struct. 128, 474–487. https://doi.org/10.1016/J.ENGSTRUCT.2016.09.060.

Cheynet, E., Jakobsen, J.B., Snæbjörnsson, J., 2019. Flow distortion recorded by sonic anemometers on a long-span bridge: towards a better modelling of the dynamic wind load in full-scale. J. Sound Vib. 450, 214–230. https://doi.org/10.1016/j.jsv.2019.03.013.

Cheynet, E., Liu, S., Ong, M.C., Jakobsen, J.B., Snæbjörnsson, J., Gatin, I., 2020. The influence of terrain on the mean wind flow characteristics in a fjord. J. Wind Eng. Ind. Aerod. 205, 104331. https://doi.org/10.1016/j.jweia.2020.104331.

Davenport, A., 1961a. The application of statistical concepts to the wind loading of structures. Proc. Inst. Civ. Eng. 19, 449–472. https://doi.org/10.1680/iicep.1961.11304.

Davenport, A.G., 1961b. The spectrum of horizontal gustiness near the ground in high winds. Q. J. R. Meteorol. Soc. 87, 194–211. https://doi.org/10.1002/qj.49708737208.

Dellwik, E., Bingöl, F., Mann, J., 2014. Flow distortion at a dense forest edge. Q. J. R. Meteorol. Soc. 140, 676–686. https://doi.org/10.1002/qj.2155.

Drobinski, P., Carlotti, P., Newsom, R.K., Banta, R.M., Foster, R.C., Redelsperger, J.-L., 2004. The structure of the near-neutral atmospheric surface layer. J. Atmos. Sci. 61, 699–714. https://doi.org/10.1175/1520-0469(2004)061¡0699:TSOTNA¿2.0.CO;2.

Dyrbye, C., Hansen, S.O., 1997. Wind Loads on Structures.

En 1991-1-4, 2005. Eurocode 1. Actions on Structures–Part 1-4: General Actions – Wind actions.. Technical Report [Authority: the European Union Per Regulation 305/2011, Directive 98/34/EC, Directive 2004/18/EC].

ESDU, 2001. Characteristics of Atmospheric Turbulence Near the Ground–Part Ii: Single Point Data for Strong Winds (Neutral Atmosphere). Engineering Sciences Data Unit, IHS Inc., London, UK. Report No. ESDU, 85020.

Fenerci, A., Øiseth, O., 2018. Site-specific data-driven probabilistic wind field modeling for the wind-induced response prediction of cable-supported bridges. J. Wind Eng. Ind. Aerod. 181, 161–179. https://doi.org/10.1016/j.jweia.2018.09.002.

Fenerci, A., Øiseth, O., Rønnquist, A., 2017. Long-term monitoring of wind field characteristics and dynamic response of a long-span suspension bridge in complex terrain. Eng. Struct. 147, 269–284. https://doi.org/10.1016/j.engstruct.2017.05.070.

Figueroa-Espinoza, B., Salles, P., 2014. Local monin–obukhov similarity in heterogeneous terrain. Atmos. Sci. Lett. 15, 299–306. https://doi.org/10.1002/asl2.503.

de Franceschi, M., Zardi, D., Tagliazucca, M., Tampieri, F., 2009. Analysis of second-order moments in surface layer turbulence in an Alpine valley. Q. J. R. Meteorol. Soc. 135, 1750–1765. https://doi.org/10.1002/qj.506.

Frank, H.P., 1996. A simple spectral model for the modification of turbulence in flow over gentle hills. Boundary-Layer Meteorol. 79, 345–373. https://doi.org/10.1007/BF00119404.

Fujino, Y., 2018. Vibration-based monitoring for performance evaluation of flexible civil structures in Japan. Proceedings of the Japan Academy, Series B 94, 98–128. https://doi.org/10.2183/pjab.94.008.

Furevik, B.R., Ágústson, H., Lauen Borg, A., Zakari, M., Nyhammer, F., Gausen, M., 2020. Meteorological observations in tall masts for mapping of atmospheric flow in Norwegian fjords. Earth Syst. Sci. Data Discuss. 1–28. https://doi.org/10.5194/essd-2020-32.

Hoffmann, K., Srouji, R., Hansen, S., 2017. Wind effects on long-span bridges: probabilistic wind data format for buffeting and VIV load assessments. MS&E 276, 012005. https://doi.org/10.1088/1757-899X/276/1/012005.

Högström, U., Hunt, J., Smedman, A.-S., 2002. Theory and measurements for turbulence spectra and variances in the atmospheric neutral surface layer. Boundary-Layer Meteorol. 103, 101–124. https://doi.org/10.1023/A:1014579828712.

Højstrup, J., 1981. A simple model for the adjustment of velocity spectra in unstable conditions downstream of an abrupt change in roughness and heat flux. Boundary-Layer Meteorol. 21, 341–356. https://doi.org/10.1007/BF00119278.

Hui, M., Larsen, A., Xiang, H., 2009. Wind turbulence characteristics study at the Stonecutters bridge site: Part – II wind power spectra, integral length scales and coherences. J. Wind Eng. Ind. Aerod. 97, 48–59. https://doi.org/10.1016/J.JWEIA.2008.11.003.

Hunt, J.C., Carlotti, P., 2001. Statistical structure at the wall of the high Reynolds number turbulent boundary layer. Flow, Turbul. Combust. 66, 453–475. https://doi.org/10.1023/A:1013519021030.

Hunt, J.C., Morrison, J.F., 2000. Eddy structure in turbulent boundary layers. Eur. J. Mech. B Fluid 19, 673–694. https://doi.org/10.1016/S0997-7546(00)00129-1.

Iyengar, A.K., Farell, C., 2001. Experimental issues in atmospheric boundary layer simulations: roughness length and integral length scale determination. J. Wind Eng. Ind. Aerod. 89, 1059–1080. https://doi.org/10.1016/S0167-6105(01)00099-X.

Kaimal, J.C., Finnigan, J.J., 1994. Atmospheric Boundary Layer Flows: Their Structure and Measurement. Oxford University Press.

Kaimal, J.C., Wyngaard, J.C., Izumi, Y., Coté, O.R., 1972. Spectral characteristics of surface-layer turbulence. Q. J. R. Meteorol. Soc. 98, 563–589. https://doi.org/10.1002/qj.49709841707.

Kanda, J., 1983. Reliability of gust response prediction considering height dependent turbulence parameters. J. Wind Eng. Ind. Aerod. 14, 455–466. https://doi.org/10.1016/0167-6105(83)90046-6.

Kanda, J., Royles, R., 1978. Further consideration of the height dependence of root-coherence in the natural wind. Build. Environ. 13, 175–184. https://doi.org/10.1016/0360-1323(78)90041-0.

von Kármán, T., 1948. Progress in the statistical theory of turbulence. Proc. Natl. Acad. Sci. U. S. A 34, 530.

Klipp, C., 2018. Turbulent friction velocity calculated from the Reynolds stress Tensor. J. Atmos. Sci. 75, 1029–1043. https://doi.org/10.1175/JAS-D-16-0282.1.

Klipp, C.L., Adelphi, M., 2008. A new scaling term for use in roughness sublayers. In: 18th Symp. On Boundary Layers and Turbulence, Stockholm, Sweden (9-13 June 2008). American Meteorological Society.

Kolmogorov, A.N., 1941. The local structure of turbulence in incompressible viscous fluid for very large Reynolds numbers. Proceedings of the USSR Academy of Sciences 30, 299–303. https://doi.org/10.1098/rspa.1991.0075.

Kristensen, L., Jensen, N.O., 1979. Lateral coherence in isotropic turbulence and in the natural wind. Boundary-Layer Meteorol. 17, 353–373. https://doi.org/10.1007/BF00117924.

Kristensen, L., Panofsky, H.A., Smith, S.D., 1981. Lateral coherence of longitudinal wind components in strong winds. Boundary-Layer Meteorol. 21, 199–205. https://doi.org/10.1007/BF02033937.

Larose, G., Zasso, A., Melelli, S., Casanova, D., 1998. Field measurements of the wind-induced response of a 254 m high free-standing bridge pylon. J. Wind Eng. Ind. Aerod. 74, 891–902. https://doi.org/10.1016/S0167-6105(98)00081-6.

Mann, J., 1994. The spatial structure of neutral atmospheric surface-layer turbulence. J. Fluid Mech. 273, 141–168. https://doi.org/10.1017/S0022112094001886.

Midjiyawa, Z., Cheynet, E., Reuder, J., Ágústsson, H., Kvamsdal, T., 2021. Potential and challenges of wind measurements with met-masts in complex terrain for bridge design: Part – I Integral flow characteristics. J. Wind Eng. Ind. Aerod. https://doi.org/10.1016/j.jweia.2021.104584. In press.

Mikkelsen, T., Larsen, S.E., Jørgensen, H.E., Astrup, P., Larsén, X.G., 2017. Scaling of turbulence spectra measured in strong shear flow near the earth's surface. Phys. Scripta 92, 124002. https://doi.org/10.1088/1402-4896/aa91b2.

Monin, A.S., Obukhov, A.M., 1954. Basic laws of turbulent mixing in the surface layer of the atmosphere. Proceedings of the Geophysical Institute USSR Academy of Sciences 24, 163–187.

Morfiadakis, E., Glinou, G., Koulouvari, M., 1996. The suitability of the von karman spectrum for the structure of turbulence in a complex terrain wind farm. J. Wind Eng. Ind. Aerod. 62, 237–257. https://doi.org/10.1016/S0167-6105(96)00059-1.

Norwegian Public Road Administration, 2015. N400 Handbook for Bridge Design. Directorate of Public Roads. https://www.vegvesen.no//865860/binary/1030718.

Ogawa, K., Matsumoto, M., Kitazawa, M., Yamasaki, T., 1990. Aerodynamic stability of the tower of a long-spanned cable-stayed bridge (Higashi-Kobe Bridge). J. Wind Eng. Ind. Aerod. 33, 349–358. https://doi.org/10.1016/0167-6105(90)90050-M.

Panofsky, H., Larko, D., Lipschutz, R., Stone, G., Bradley, E., Bowen, A.J., Højstrup, J., 1982. Spectra of velocity components over complex terrain. Q. J. R. Meteorol. Soc. 108, 215–230. https://doi.org/10.1002/qj.49710845513.

Panosfsky, H., Dutton, J., 1984. Atmospheric Turbulence: Models and Methods for Engineering Applications. JohnWiley&Sons, NewYork.

Peña, A., Dellwik, E., Mann, J., 2019. A method to assess the accuracy of sonic anemometer measurements. Atmospheric Measurement Techniques 12, 237–252. https://doi.org/10.5194/amt-12-237-2019.

Ropelewski, C.F., Tennekes, H., Panofsky, H.A., 1973. Horizontal coherence of wind fluctuations. Boundary-Layer Meteorol. 5, 353–363. https://doi.org/10.1007/BF00155243.

Saranyasoontorn, K., Manuel, L., 2008. On the propagation of uncertainty in inflow turbulence to wind turbine loads. J. Wind Eng. Ind. Aerod. 96, 503–523. https://doi.org/10.1016/j.jweia.2008.01.005.

Savitzky, A., Golay, M.J., 1964. Smoothing and differentiation of data by simplified least squares procedures. Anal. Chem. 36, 1627–1639. https://doi.org/10.1021/ac60214a047.

Scanlan, R.H., 1978. The action of flexible bridges under wind, II: buffeting theory. J. Sound Vib. 60, 201–211. https://doi.org/10.1016/S0022-460X(78)80029-7.

Schlez, W., Infield, D., 1998. Horizontal, two point coherence for separations greater than the measurement height. Boundary-Layer Meteorol. 87, 459–480. https://doi.org/10.1023/A:1000997610233.

Shaw, R.H., Tavangar, J., Ward, D.P., 1983. Structure of the Reynolds stress in a canopy layer. J. Clim. Appl. Meteorol. 22, 1922–1931. https://doi.org/10.1175/1520-0450(1983)022¡1922:SOTRSI¿2.0.CO;2.

Simiu, E., Scanlan, R.H., 1996. Wind Effects on Structures: Fundamentals and Applications to Design, third ed. John Wiley, New York.

Solari, G., Piccardo, G., 2001. Probabilistic 3-D turbulence modeling for gust buffeting of structures. Probabilist. Eng. Mech. 16, 73–86. https://doi.org/10.1016/S0266-8920(00)00010-2.

Song, J.-L., Li, J.-W., Flay, R.G., 2020. Field measurements and wind tunnel investigation of wind characteristics at a bridge site in a y-shaped valley. J. Wind Eng. Ind. Aerod. 202, 104199. https://doi.org/10.1016/j.jweia.2020.104199.

Sorbjan, Z., 1986. On similarity in the atmospheric boundary layer. Boundary-Layer Meteorol. 34, 377–397. https://doi.org/10.1007/BF00120989.

Soucy, R., Woodward, R., Panofsky, H., 1982. Vertical cross-spectra of horizontal velocity components at the boulder observatory. Boundary-Layer Meteorol. 24, 57–66. https://doi.org/10.1007/BF00121799.

Tieleman, H.W., 1995. Universality of velocity spectra. J. Wind Eng. Ind. Aerod. 56, 55–69. https://doi.org/10.1016/0167-6105(94)00011-2.

Wang, J., Cheynet, E., Snæbjörnsson, J., Jakobsen, J.B., 2018. Coupled aerodynamic and hydrodynamic response of a long span bridge suspended from floating towers. J. Wind Eng. Ind. Aerod. 177, 19–31. https://doi.org/10.1016/j.jweia.2018.03.024.

Wardlaw, R., 1990. Wind effects on bridges. J. Wind Eng. Ind. Aerod. 33, 301–312. https://doi.org/10.1016/0167-6105(90)90045-E.

Weber, R.O., 1999. Remarks on the definition and estimation of friction velocity. Boundary-Layer Meteorol. 93, 197–209. https://doi.org/10.1023/A:1002043826623.

Welch, P., 1967. The use of fast fourier transform for the estimation of power spectra: a method based on time averaging over short, modified periodograms. IEEE Trans. Audio Electroacoust. 15, 70–73. https://doi.org/10.1109/TAU.1967.1161901.

Yu, B., Gan Chowdhury, A., Masters, F.J., 2008. Hurricane wind power spectra, cospectra, and integral length scales. Boundary-Layer Meteorol. 129, 411–430. https://doi.org/10.1007/s10546-008-9316-8.

Yu, C., Li, Y., Zhang, M., Zhang, Y., Zhai, G., 2019. Wind characteristics along a bridge catwalk in a deep-cutting gorge from field measurements. J. Wind Eng. Ind. Aerod. 186, 94–104. https://doi.org/10.1016/j.jweia.2018.12.022.